Expanding the DNA damaging potential of artificial metallo-nucleases with click chemistry

nature communications

Article

https://doi.org/10.1038/s41467-026-68911-5

Expanding the DNA damaging potential of artificial metallo-nucleases with click chemistry

Received: 31 March 2025

Accepted: 20 January 2026

Published online: 03 February 2026

Check for updates

Alex Gibney[1], Margareth Sidarta[2,3], Eva Delahunt[1], Pierre Mesdom[4], Lily Arrué[5,6], Sriram KK[2,3], Obed Akwasi Aning[2], Hedvig Hjerpe[7,8], Francisca Figueiredo[4], Kevin Cariou[4], Vickie McKee[1,9], Pegah Johansson[7,8], Shayon Bhattacharya[5], Damien Thompson[5], Michaela Wenzel[2,3], Gilles Gasser[4], Fredrik Westerlund[2,3] & Andrew Kellett[1]

Recently, copper(I)-catalysed azide-alkyne cycloaddition (CuAAC) click chemistry has emerged as a promising approach for designing new artificial metallo-nucleases (AMNs) with DNA-damaging properties. By functionalising a central organic azide with three alkyne donors, Tri-Click (TC) ligands capable of chelating three copper ions through the donor group and triazole linker can be generated. However, the versatility of this approach along with the influence of specific donors on metal binding, DNA recognition, and cellular DNA damage in an anticancer context remains poorly understood. Here, we prepare a series of Tri-Click ligands incorporating systematic cyclic and acyclic N-, O-, and S-donors and evaluate their AMN activities. Screening experiments pinpoint planar N-donor ligands as high value agents. Among these, the copper complex of Tri-Click-Pyridine (Cu_3-TC-Py) displays significant potential. We characterise its activity using single-molecule imaging, microscale thermophoresis, FRET-based binding assays, molecular dynamics, and intracellular DNA interaction studies in human and functional bacterial cells. We report the emergence of Cu_3-TC-Py as a lead AMN with high reactivity for DNA damage applications central to anticancer therapy.

The copper(I)-catalysed azide-alkyne cycloaddition (CuAAC) and strain-promoted azide-alkyne cycloaddition (SPAAC) reactions were recognised by the 2022 Nobel prize in chemistry as fundamental advancements in functional chemistry[1–5]. In medicinal chemistry, the CuAAC reaction primarily serves as a fast and efficient method for creating complex molecules[6–10]. However, the 1,2,3-triazole generated during this reaction has distinctive properties, including sp^2-hybridised nitrogen atoms capable of forming coordination bonds with transition metals. Click chemistry therefore serves as a valuable tool for the development of coordinating ligands[11–13]. We recently demonstrated that click chemistry could be used to efficiently prepare new metallodrug candidates from simple, inert starting materials[14–17]. This

[1]Research Ireland Centre for Pharmaceuticals, School of Chemical Sciences, Dublin City University, Dublin, Ireland. [2]Department of Life Sciences, Chalmers University of Technology, Gothenburg, Sweden. [3]Centre for Antibiotic Resistance Research in Gothenburg (CARe), Gothenburg, Sweden. [4]Chimie ParisTech, PSL Université, CNRS, Institute of Chemistry for Life and Health Sciences, Paris, France. [5]Research Ireland Centre for Pharmaceuticals, Department of Physics, University of Limerick, Limerick, Ireland. [6]Department of Chemistry, Nanoscience Center, University of Jyväskylä, Jyväskylä, Finland. [7]Department of Clinical Chemistry, Sahlgrenska University Hospital, Region Vastra Gotaland, Gothenburg, Sweden. [8]Department of Laboratory Medicine, Institute of Biomedicine, Sahlgrenska Academy at University of Gothenburg, Gothenburg, Sweden. [9]Department of Physics, Chemistry and Pharmacy, University of Southern Denmark, Odense, Denmark. e-mail: andrew.kellett@dcu.ie

https://doi.org/10.1038/s41467-026-68911-5

concept is exemplified by the Tri-Click (TC) ligands (Fig. 1a), characterised for their ability to coordinate up to three copper(II) ions that promote DNA damage. These agents belong to a class of metal complex that oxidatively cleaves DNA, known as artificial metallo-nucleases (AMNs), which offer therapeutic potential due to their metallo-bleomycin-like activity[18,19]. Our first study reporting the synthesis of TC-1 revealed the positioning of the secondary donor relative to the 1,2,3-triazole group was vital to copper binding and DNA reactivity[14]. Recent work then identified TC-Thio as a promising ligand that introduced aromaticity and Cu(I) accessibility through a sulfur donor, ethynylthiophene[15]. However, the influence of different alkyne donors on metal binding, DNA recognition, and oxidative DNA damage remains poorly understood. Here, we report the addition of a series of aromatic and aliphatic N-, O- and S- donors into the Tri-Click scaffold with the aim of identifying properties favourable to copper-sensitised DNA binding and reactivity in biological systems with particular focus on anticancer applications.

Results

Series design and preparation

New TC ligands were designed to contain a secondary donor proximal to the 1,2,3-triazole to create suitable metal ion chelators. Previous studies show that a three-bond spacer between the terminal alkyne and the secondary donor, such as that found in propargyl amine or 2-ethynyl thiophene (Fig. 1a), is suited for this purpose. Therefore, we selected a diverse range of propargyl and heteroaromatic 2-ethynyl starting materials for CuAAC coupling with a *tris*(azidomethyl)-mesitylene (triazide) core (Supplementary Fig. 1). The set of ligands contain

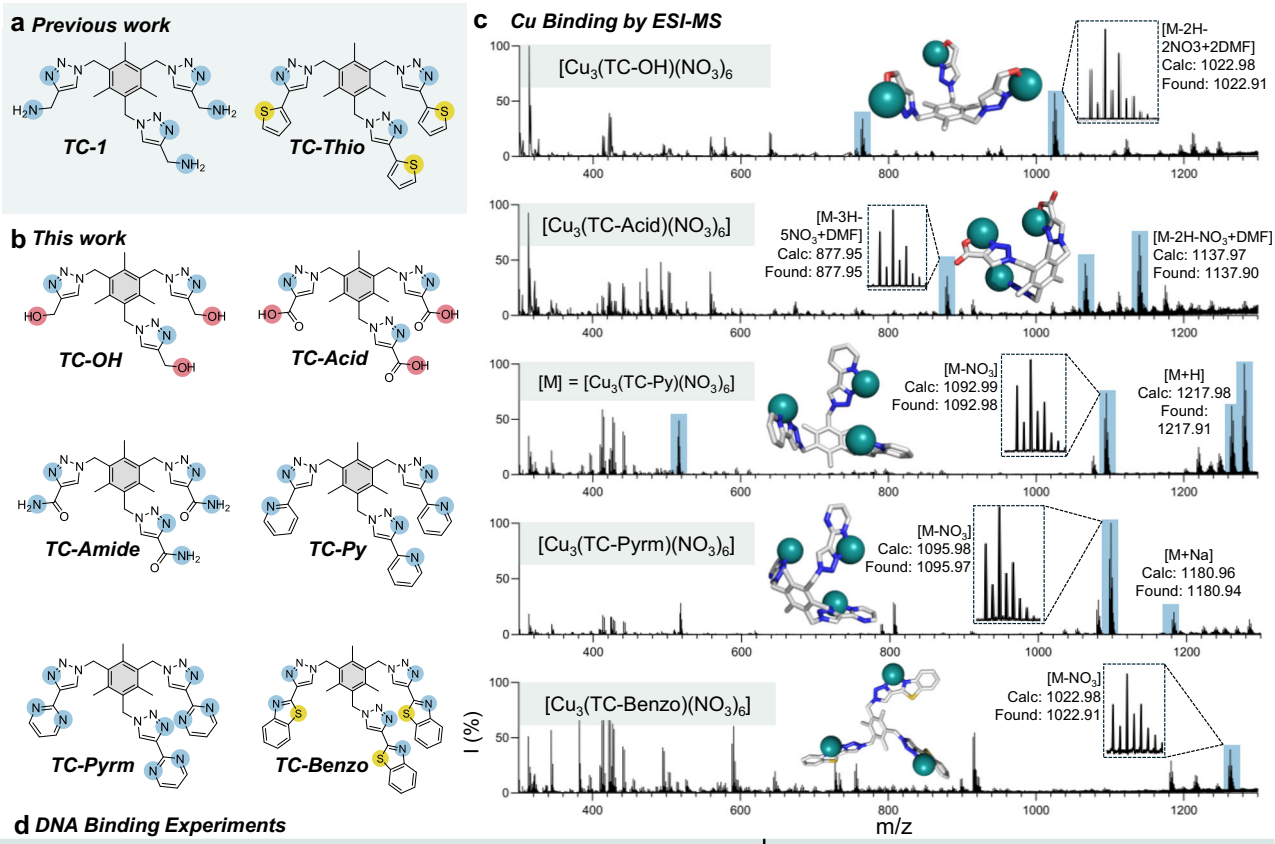

d *DNA Binding Experiments*

Complex	Binding affinity (saturation)		Binding mode (limited fluorophore)	
	C_{50} (μM)	K_{app} (M^{-1})	$Q_{Hoechst}$ (μM)	Q_{MG} (μM)
Cu_3-TC-OH	16.1 ± 0.1	6.8 x 10^6	91.67 ± 14.1	206.7 ± 38.3
Cu_3-TC-Acid	13.3 ± 0.1	8.3 x 10^6	89.19 ± 13.7	183.0 ± 32.5
Cu_3-TC-Pyrm	7.8 ± 0.1	1.4 x 10^7	13.2 ± 0.7	23.8 ± 1.8
Cu_3-TC-Py	1.9 ± 0.2	5.8 x 10^7	12.0 ± 1.2	22.7 ± 1.5
Cu_3-TC-Benzo	30.2 ± 0.1	3.6 x 10^6	69.32 ± 6.3	181.6 ± 22.3

Fig. 1 | Molecular structures, ESI-MS profiles with copper(II) ions, and DNA recognition properties of new TC ligands. a Molecular structures of earlier reported TC-1 and TC-Thio ligands[14,15]. **b** Molecular structures of six new TC ligands reported in this study where the alkyne donors give rise to a variety of aliphatic and heteroaromatic copper(II) binding groups. **c** TC ligands form trinuclear Cu complexes as identified using electrospray ionisation-mass spectrometry (ESI-MS) analyses. Identifiable fragments are shown in blue and the full list of fragments, their masses and comparisons of calculated versus found masses are available Supplementary Table 3. Inset is a simple molecular model of the expected structure less counterions. [M] indicates the assumed molecular ion. **d** Competitive DNA binding and quenching experimental results with calf thymus DNA (ctDNA). C_{50}, $Q_{Hoechst}$, and Q_{MG}, are the concentrations of Cu_3-TC complex required to reduce the respective fluorescence of bound ethidium bromide (EtBr), Hoechst 34580, and methyl green (MG) by 50%. EtBr was used in excess to calculate the apparent DNA binding constant (K_{app}), while limited concentrations of Hoechst 34580 and MG were employed to identify preferential binding mode. All error bars indicate the standard error of the mean observed between three biological replicates ($n = 3$).

weak and strong donors, varied steric constrains, and planar structural motifs. Commercially available alkyne starting materials were selected from: propargyl alcohol, propiolic acid, propiolamide, 2- ethynylpyrimidine, 2-ethynylpyridine, and 2-ethynylbenzothiazole. Each of the alkyne donors were then reacted via CuAAC with the triazide core, resulting in TC-OH, TC-Acid, TC-Amide, TC-Pyrm, TC-Py and TC-Benzo, respectively (Fig. 1b). All ligand syntheses proceeded readily in benign solvents, with high yields that required simple, non-chromatographic purification (Supplementary Fig. 2–19).

Copper binding analysis

Electrospray ionisation-mass spectrometry (ESI-MS) was used to characterise the Cu(II) binding properties of each TC ligand (Fig. 1c and Supplementary Table 3). Spectra of samples containing TC ligands with three molar equivalents of Cu(II) nitrate trihydrate in a 50:50 water:dimethyl formamide solution were recorded and compared to the theoretical patterns expected for an assumed molecular structure with the general formula $[Cu_3(TC)(NO_3)_6]$ (M). Trinuclear complexes were identified for singly and doubly charged ions with isotope patterns arising from the natural ^{63}Cu /^{65}Cu abundances. All spectra indicated the presence of trinuclear Cu(II) complexes, except for the TC-Amide sample, which was not further investigated. The spectra of heteroaromatic ligands TC-Pyrm and TC-Benzo showed mono-cationic $[M\text{-}NO_3]^+$ formation due to the loss of a single nitrate anion, while TC-Pyrm showed additional evidence for the loss of a second nitrate $[M\text{-}2(NO_3)]^{2+}$. The TC-OH and TC-Acid spectra required more complex analysis and the compounds likely exist as an equilibrium mixture between the free ligand and complex. Mono- and di-cationic ions of Cu_3-TC-Py, $[M\text{-}NO_3]^+$ and $[M\text{-}2(NO_3)]^{2+}$, were detected along with hydrogen and nitric acid adducts ($[M+H]^+$ and $[M+HNO_3]^+$), which were not observed for any other TC sample, indicating potentially improved solution stability of this complex. The ESI-MS spectrum for Cu_3-TC-Py provided no evidence of mono- or di-copper(II) complexes forming in tandem with the trinuclear complex. To corroborate these findings, a UV-vis analysis was performed by adding $Cu(NO_3)_2$ to a fixed, 100 µM solution of TC-Py and monitoring the change in absorbance between 270 and 800 nm (Supplementary Fig. 20). Plotting of absorbance at 283 nm vs stoichiometric equivalents of $Cu(NO_3)_2$ showed a clear hyperchromic trend with an inflection point calculated at 2.93 equivalents of $Cu(NO_3)_2$, further supporting the formation of the trinuclear complex, Cu_3-TC-Py.

DNA recognition

Next, the DNA binding properties of the Cu_3-TC complexes were investigated using **1)** a competition assay with the DNA intercalating fluorophore ethidium bromide (EtBr), and **2)** quenching experiments using limited bound fluorophores Hoechst-34580 (Hoechst) and methyl green (MG)[20], which bind in the minor and major grooves of DNA, respectively (Fig. 1d and Supplementary Fig. 21). In the competition study, EtBr was added in excess to calf thymus DNA (ctDNA) and titrated Cu_3-TC complexes were observed to efficiently displace EtBr with C_{50} values (the concentration required to reduce fluorescence by 50%) ranging from 2–30 µM (where the EtBr concentration was 12.5 µM). The C_{50} values were then used to calculate apparent DNA binding constants via a derivative of the Cheng-Prusoff equation: $K_{app} = (8.8 \times 10^6\ M^{-1})(12.5/C_{50})$, where $8.8 \times 10^6\ M^{-1}$ is the binding constant of EtBr, 12.5 is the micromolar concentration of EtBr, and K_{app} is the apparent binding constant of the analyte[21]. The K_{app} values ranged from 3.6×10^6 to $5.8 \times 10^7\ M^{-1}$. Within these results, both Cu_3-TC-Pyrm and Cu_3-TC-Py stood out at the upper end of the series. Next, fluorescence quenching assays with Hoechst and MG, conducted under limited bound conditions with ctDNA, showed that the minor groove-binding Hoechst was more efficiently quenched compared to the major groove-binding MG; in all cases, the Q_{MG} value (where Q is the analyte concentration required to reduce the intrinsic fluorescence by 50%) was approximately double that of $Q_{Hoechst}$. Cu_3-TC-Py most efficiently displaced both fluorophores, closely followed by the structurally similar Cu_3-TC-Pyrm. Overall, these data suggest that the Cu_3-TC complexes are selective for the minor groove of duplex DNA and that heteroaromatic N,N donors provide enhanced DNA recognition properties.

DNA hairpin binding analysis

Due to the favourable results obtained for Cu_3-TC-Py in the ESI-MS, UV-vis, and DNA binding experiments, this complex was selected for in-depth analysis using microscale thermophoresis (MST) and Förster resonance energy transfer (FRET) melting. Here, palindromic DNA hairpins containing the Dickerson-Drew (DD) consensus sequence separated by an internal five-nucleotide adenine (A) loop were designed (Supplementary Fig. 22). The first hairpin (F-DDH) contained a 5′-Alexa Fluor™ 647 N modification that facilitated MST measurements, while the second hairpin (FRET-DDH) contained a FRET pair consisting of 3′-Iowa Black® and 5′-Alexa Fluor™ 647 labels. MST measures changes in the movement of an analyte along a microscopic temperature gradient (thermophoresis) due to changes in size, shape, charge, or hydration shell of the fluorescently labelled target upon binding[22–24]. Analysis of F-DDH in the presence of increasing concentrations of Cu_3-TC-Py showed a typical MST profile with clear unbound and bound MST trace populations at low titrant concentration (Fig. 2a). However, at high concentrations the MST traces lost resolution and became irregular. Examination of the initial intensity values (the fluorescence of the sample prior to heating) showed a clear dose-dependent decrease, indicating that Cu_3-TC-Py was likely condensing the hairpin. An overlay of the normalised MST trace values at $t = 5$ s ($FNorm_5$) and the initial intensity values allowed us to clearly differentiate the binding and the non-specific condensation phases. The $FNorm_5$ plot gradually increases with titrated Cu_3-TC-Py, before a sharp inflection point and subsequent decrease that aligns well with the condensation profile shown in the initial intensity plot. The shared inflection point at 1.8 equivalents of Cu_3-TC-Py suggests a binding site of approximately 6 base pairs. Nonlinear regression of the binding region gave a K_d of 430 nM and that of the condensation region gave an EC_{50} of 9 µM. FRET melting showed a similar trend to that of the MST experiments. Here, the normalised melting curves show two distinct phases, which were assigned to discrete binding and condensation phases; the first phase represents increasing thermal stability of the hairpin upon complex binding, while the second phase represents dissolution of larger DNA condensates. Plotting the observed T_m values clearly demonstrates these two phases (Fig. 2b). The binding region here shows saturation at $r \approx 1.8$ (where r = [complex]/[DNA]), and a K_d of 690 nM, in strong agreement with the MST data. Fitting the MST data with the Bard equation (Supplementary Fig. 23) returned an intrinsic binding constant (K_b) of $1.9 \times 10^7\ M^{-1}$ and a 2:1 Cu_3-TC-Py:F-DDH binding stoichiometry[25]. Applying this same model to the FRET melting data returned a $K_b = 9.2 \times 10^6\ M^{-1}$ (Supplementary Fig. 24) with the same binding stoichiometry as the MST analysis suggesting Cu_3-TC-Py occupies a binding site of 6 base pairs. Finally, both K_b values are in general agreement with the earlier calculated K_{app} value and corroborate Cu_3-TC-Py as high-affinity DNA binding agent.

We next employed the FRET melting assay within a wider panel of hairpin sequences to identify preferential groove or sequence context binding by Cu_3-TC-Py. Here, we designed a number of DNA hairpins with varying groove accessibilities, and GC content, along with base pair mismatches (Fig. 2c and Supplementary Fig. 25) for analysis. We first modified the DDH sequence to contain 5-methyl cytosine (MDDH) or uracil (UDDH) bases in place of cytosine and thymine, respectively. The methyl group of 5-methyl cytosine reduces steric accessibility to the major groove, while the absence of the methyl group in uracil (compared to thymine) increases the accessibility of the major

https://doi.org/10.1038/s41467-026-68911-5

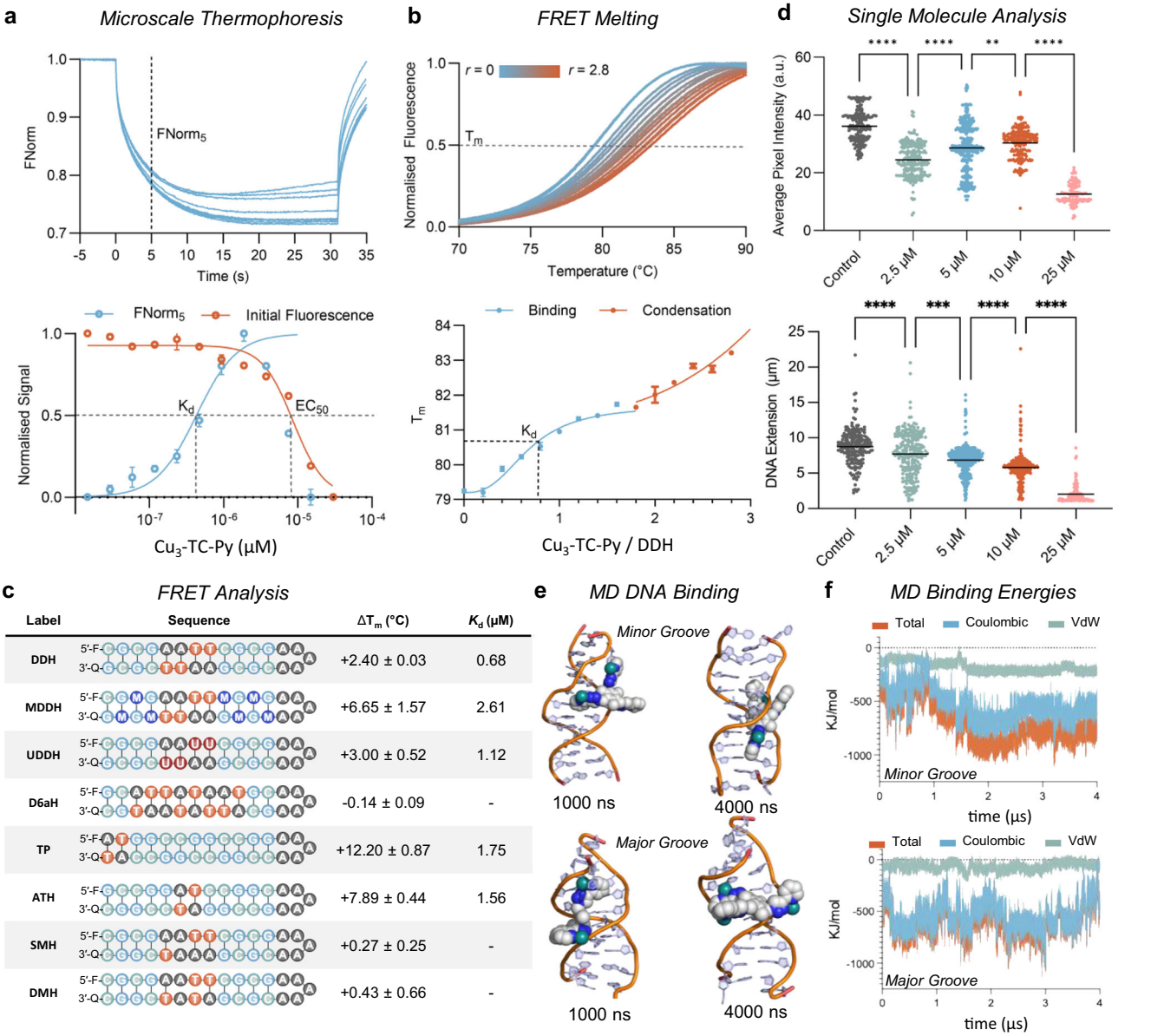

Fig. 2 | Detailed DNA binding studies of Cu_3-TC-Py. a MST traces showing two binding populations for Cu_3-TC-Py–DNA interactions; FNorm5 (blue) and initial intensity (orange) were used to derive K_d and C_{50} values. Data are presented as mean ± SEM. **b** Fluorescence melting of hairpin DNA showing progressive T_m increases with added complex; K_d obtained from T_m versus equivalents plot. The plot shows the assigned binding (blue) and condesnation regions (orange). Data are presented as mean ± SEM. **c** Summary table of fluorescence melting results assessing sequence and groove selectivity of Cu_3-TC-Py (M = 5-mC, U = uracil; T_m max = maximum shift before condensation). **d** Nanofluidic single-molecule imaging of YOYO-1–stained λ-DNA showing changes in pixel intensity and contour length. **e** Molecular-dynamics snapshots of Cu_3-TC-Py bound in DNA grooves (top = major; bottom = minor). **f** Time-resolved binding energies from simulations shown in (**e**) (top = minor groove; bottom = major groove). Orange = total, blue = coulombic and green = Van der Waals.

groove[26]. Cu_3-TC-Py induced thermal melting changes (ΔT_m) of +6.65 °C for MDDH and +3.00 °C for UDDH with corresponding K_d values of 2.61 and 0.68 μM, respectively. Together these results indicate that Cu_3-TC-Py can bind both DNA grooves with high affinity but minor groove residency results in greater thermodynamic stabilisation of the duplex.

Next, to investigate the sequence selectivity of Cu_3-TC-Py, we used hairpins with varying sequence contexts. The D6aH and TP hairpins provided targets with low and high GC content, respectively. Here, Cu_3-TC-Py produced a ΔT_m of +12.20 °C for the TP sequence but had negligible impact on the melting temperature of D6AH, suggesting a high preference for GC rich tracts. To evaluate if the thermodynamic stabilisation of TP was due to specific binding within a contiguous GC-rich tract, experiments with the ATH hairpin, which contains a central AT/AT step flanked by GC rich regions, were performed. Although Cu_3-TC-Py significantly stabilised the ATH sequence, the ΔT_m value (+7.89 °C) was lower than TP. Finally, we designed DDH analogues containing single- (SMH) and double-mismatches (DMH) to investigate if Cu_3-TC-Py could bind via metalloinsertion–a binding mode distinctive to intercalation, that causes the ejection of mismatched bases induced by a portion of a bulky metal complex sitting directly within the DNA helix[27–29]. Here, we found that both the single- and double-mismatches completely negated the thermal stabilisation provided by Cu_3-TC-Py, ruling out metalloinsertion as a potential binding mode. Overall, these FRET-based thermal melting experiments suggest that Cu_3-TC-Py shows a significant degree of selectivity for the minor groove of GC-rich DNA, with limited tolerance for DNA mismatches or AT-rich tracts within the binding region.

Single-molecule DNA analysis

In order to directly probe structural changes imposed on DNA by Cu_3-TC-Py, single-molecule images of ~50 kbp long λ-DNA molecules exposed to the complex were taken using fluorescence microscopy for DNA confined in nanofluidic channels[30]. By comparing DNA molecules in samples with increasing Cu_3-TC-Py, trends related to DNA length and fluorescence intensity could be plotted to yield relative distribution profiles. The DNA was visualised by incubating the DNA with the Cu_3-TC-Py prior to addition of YOYO-1, followed by fluorescence imaging in the nanofluidic channels. YOYO-1 is a bis-intercalating fluorescent dye that extends the length of the DNA helix[31–33]. Saturating the DNA molecules with YOYO-1 therefore ensures DNA molecules are maximally stretched, with the highest possible fluorescence intensity. Change in either DNA extension or intensity can then be directly monitored upon exposure to an analyte, such as Cu_3-TC-Py. Staining of λ-DNA, pretreated with 2.5 μM Cu_3-TC-Py decreased the average pixel intensity observed relative to the untreated control, indicating that Cu_3-TC-Py competes with YOYO-1 binding at this concentration (Fig. 2d). The intensity values then increase somewhat in samples treated with 5 and 10 μM Cu_3-TC-Py before reaching a minimum at 25 μM of Cu_3-TC-Py. It appears the initial reduction in intensity is due to displacement of YOYO-1 via direct competitive DNA binding by the complex, while recovery at 5 and 10 μM occurs due to non-competitive binding events that cause the DNA to contract, increasing the YOYO-1 density per pixel. Saturating λ-DNA with 25 μM of the complex causes complete DNA condensation and a dramatic decrease in YOYO-1 emission. This is supported by DNA extension plots which show a steady decrease in λ-DNA molecule length with increasing Cu_3-TC-Py and complete condensation at 25 μM and also total fluorescence plots (Supplementary Fig. 26) that show a sharp decrease (indicating YOYO-1 ejection) at 2.5 μM Cu_3-TC-Py which remains constant up to 10 μM Cu_3-TC-Py. The single-molecule data are in excellent agreement with earlier hairpin and quenching analysis suggesting two distinct DNA interaction phases: minor groove binding, and non-specific electrostatic effects resulting in DNA condensation.

Molecular docking

To evaluate the minor groove binding properties further, molecular docking studies of Cu_3-TC-Py with the Dickerson-Drew dodecamer (DDD, PDB code 1BNA) were performed. We began by generating a model of Cu_3-TC-Py using classical mechanics in Avogadro and optimising this to an energy minimum[34]. The resulting structure was then added to a grid box that encapsulated the entire DDD target for docking. Here, Cu_3-TC-Py was found to bind predominantly in the minor groove with eight of the nine docking output poses showing minor groove residency and one pose showing a major groove binding (Supplementary Fig. 27). We next sought to investigate the saturation characteristics of Cu_3-TC-Py binding by taking the top ranked pose from the docking with 1BNA and treating this entire complex as a rigid macromolecule for a second round of docking with another molecule of Cu_3-TC-Py (Supplementary Fig. 28). All output poses placed the second Cu_3-TC-Py molecule in the major groove of the duplex.

Molecular dynamics

To provide greater depth on the binding mode of Cu_3-TC-Py, MD simulations of the DDD were undertaken using the highest affinity major and minor groove docking poses as starting positions. Figure 2e shows still frames of the minor and major groove simulations. First, both MD simulations show that the Cu_3-TC-Py complex remains bound within the starting groove of the duplex, supporting earlier findings that the complex is a high-affinity DNA binder. A detailed discussion of MD data is provided in the supporting information. Briefly, the plateauing of the Cu_3-TC-Py RMSD (root mean square deviation) within ~2 μs indicates the formation of well-equilibrated binding poses, with small fluctuations consistent with molecular conformational shifts and dynamics in the solvated DNA-bound structures. The radius of gyration (Rg) data shows a tendency for more pronounced and abrupt transition to more compact DNA structures in the minor groove-bound structure, supporting the hypothesis of complex-induced DNA compaction during the two-phase binding/condensation process observed experimentally (Supplementary Fig. 40). To probe the binding footprint, we quantified the frequency and character of base-specific interactions across all replicates, consistently revealing engagement with six base pairs from the minor groove (Supplementary Tables 5–9), which is in excellent agreement with our earlier FRET analysis with the F-DDH sequence. Plotting the coulombic, van der Waals (vdW), and total energies versus time (Fig. 2f) then revealed that the major contributing binding force is electrostatic or coulombic interactions. Therefore, it appears that the binding interaction is driven largely by the highly cationic nature of the complex towards anionic DNA. However, although the coulombic interactions in both simulations were broadly similar, the minor groove simulation showed a significant increase in vdW interactions that supports our earlier finding of Cu_3-TC-Py binding with some selectively for the narrower minor groove. Mechanistically, two arms of the complex remain within each of the grooves while the third is ejected and interacts with the phosphate backbone.

Cytotoxicity and Cu Internalisation Studies

To compare TC-Py's broad-spectrum anticancer properties with earlier TC compounds, the free ligand was submitted alongside TC-1 and TC-Thio to the U.S. National Cancer Institute's (NCI) Developmental Therapeutics Program (DTP) 60 human cancer cell line screen. At the time of submission, conducting an NCI-60 screen of the copper complexes was not feasible due to the acceptance criteria of small molecules being limited to organic compounds. However, screening the free ligands remains important, as it may offer insights into potential prodrug activity, where the ligand could interact with bioavailable copper to promote activity[35]. The cytotoxic effects were identified initially at one-dose (10 μM) shown as a heat map in Fig. 3a. The panel consists of cell lines from a variety of cancers including leukaemia, non-small cell lung, colon, central nervous system, melanoma, ovarian, renal, prostate, and breast cancers. TC-1 was inactive and was therefore not analysed further. Both TC-Thio and TC-Py ligands displayed activity against several cell lines including triple-negative breast cancer MDA-MB-231 and MDA-MB-468, renal cancer (RXF 393), melanoma (SK-MEL-2), along with some ovarian, CNS, and non-small cell lung cancers. Both compounds were then examined using five-dose analysis within the NCI-60 panel where additional analyses to identify 50% growth inhibition (GI_{50}) were mapped (Supplementary Table 4 and Supplementary Fig. 29). Overall, both ligands were least active against the leukaemia panel but display greatest activity against ovarian cancer lines (except OVCAR-5) with heightened activity toward IGROV1, OVCAR-4, and SK-OV-3. The five-dose analysis also confirmed activity towards triple-negative breast cancers MDA-MB-231 and MDA-MB-468 with GI_{50} values ranging between 7.24 μM–20.42 μM for both ligands. Notably, growth inhibition by the free ligands does not appear to correlate directly with either labile or total intracellular Cu levels within the NCI-60 panel, as carefully characterized by Chang et al.[35]. For instance, although PC3, BT-549, and HOP-92 cells exhibit some of the highest labile intracellular Cu levels, exposure to the TC-Py ligand resulted in low micromolar GI_{50} values (14.45, 12.59, and 1.20 μM, respectively), comparable to those observed in cell lines with relatively low labile Cu, such as MCF7, T47D, and OVCAR-8 (9.12, 6.03, and 2.69 μM, respectively). While additional studies would be required to clarify the underlying processes, these findings suggest that a simple prodrug mechanism—whereby the ligands chelate intracellular Cu and elicit cytotoxicity through subsequent DNA damage—does not appear to be the dominant pathway responsible for growth inhibition by the free TC ligands.

https://doi.org/10.1038/s41467-026-68911-5

To further examine this effect, we evaluated the sensitivity of several cell lines with distinct intracellular Cu lability profiles to Cu_3-TC-Py and Cu_3-TC-Thio, alongside $CuCl_2$ as a control (Fig. 3b and Supplementary Fig. 30). In cell-based assays, $CuCl_2$ served as the copper source, and $CuCl_2$-only controls were tested at three-times the molar concentration of the Cu_3-TC complexes to ensure equivalent total Cu exposure. We selected four cell lines–PC3, DU145, A549 and MDA-MB-231–for cytotoxicity assays. PC3 exhibits a median level of total intracellular Cu but among the highest levels of labile intracellular Cu whereas DU145 displays the opposite profile, with high total but low labile levels of Cu. Both A549 and MDA-MB-231 contain relatively low levels of both Cu pools. In these assays, $CuCl_2$ alone showed no activity up to 250 μM, whereas Cu_3-TC-Py consistently produced IC_{50} values in the 10-30 μM range and Cu_3-TC-Thio in the 30-60 μM range. Notably, Cu_3-TC-Thio displayed limited toxicity toward DU145 cells within the tested range, while Cu_3-TC-Py yielded an IC_{50} of 12 μM for the same cell line. Collectively, these data indicate that Cu_3-TC-Py exhibits greater anticancer potency than Cu_3-TC-Thio across this panel.

Next, to understand the Cu uptake properties of Cu_3-TC-Py, we conducted ICP-MS experiments to measure the total Cu content in A549, MDA-MB-231, and PC3 cell lines post-treatment with Cu_3-TC-Py at 48 and 72 h (Fig. 4a). The results show that Cu_3-TC-Py significantly increased the Cu content in all cell lines at both time points, suggesting significant cellular uptake of the complex. For MDA-MB-231 and PC3 cells, a similar uptake pattern emerged where ~20 ng of Cu/million cells was found post 48 h of exposure with this level rising to ~40 ng after 72 h of exposure. A different trend emerged for A549 cells where very high Cu levels (~50 ng of Cu/per million cells) were detected after 48 h with lower levels (~30 ng) detected after 72 h, suggesting a degree of Cu efflux. Interestingly, the total uptake and overall internalisation trend observed for Cu_3-TC-Py differs significantly to Cu_3-TC-Thio (Supplementary Fig. 31) with notably higher Cu uptake facilitated by the TC-Py complex in MDA-MB-231 cells upon 72 h exposure. Finally, cell cycle analysis of MDA-MB-231 cells revealed that treatment with 25 μM Cu_3-TC-Py resulted in an increased population within the G2/M phase and a corresponding decrease in S and $G_0/_1$ phases, relative to cells treated with $CuCl_2$ alone at 75 μM (Fig. 4b). This distribution is consistent with activation of the G_2/M DNA damage checkpoint, which prevents mitosis until DNA is repaired[36–38]. In summary, these results indicate that Cu_3-TC-Py is cytotoxic and likely acts predominantly via the induction of DNA damage.

DNA damage assessment

To assess the artificial nuclease activity of Cu_3-TC-Py, electrophoresis experiments with supercoiled pUC19 DNA were undertaken. Damage to one strand of supercoiled DNA causes relaxation to the open circular conformation, while double strand breaks (DSBs)—including two proximate nicking events on the opposite strands of the helix—cause relaxation to the linear form. Since each of these forms has different topological states, damaged molecules can be distinguished and quantified by resolving their mobility using agarose electrophoresis. Triplicate experiments involving supercoiled pUC19 DNA exposed to increasing concentrations of Cu_3-TC-Py in the presence of added reductant, sodium-*L*-ascorbate, were performed. DNA damage was then visualised and quantified using band densitometry (Fig. 4c). Here, the gradual conversion from supercoiled to open circular, followed by linear forms was identified as a function of increasing Cu_3-TC-Py concentration. Notably, the formation of linear form occurs before the complete degradation of the supercoiled form (Supplementary Fig. 32). This profile is a classic indication of independent double strand break formation. To confirm DSB formation, Freifelder-Trumbo analysis was then performed (Fig. 4d).

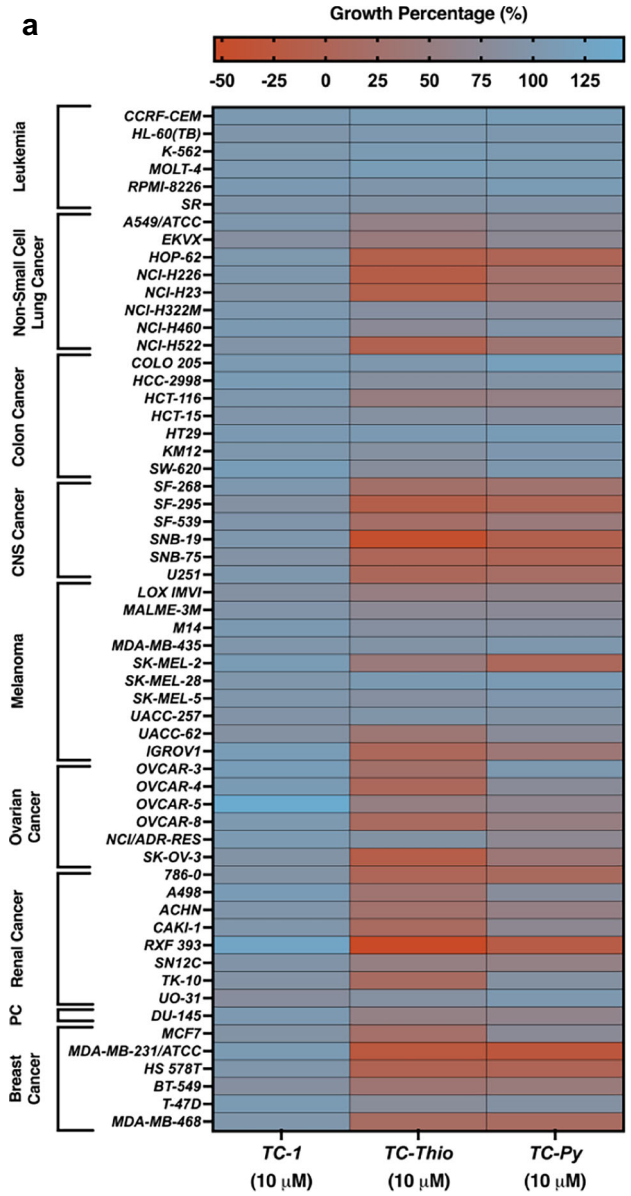

b

IC_{50} (μM)

Cell Line	$CuCl_2$	Cu_3-TC-Py	Cu_3-TC-Thio
A549	>250	29.8 ± 1.1	53.2 ± 2.0
MDA-MB-231	>300	12.7 ± 1.2	22.7 ± 1.2
PC3	>300	24.2 ± 0.8	60.1 ± 1.0
DU145	>300	12.0 ± 0.4	>100

Fig. 3 | Cytotoxicity Screening. a NCI-60 anticancer growth inhibition data of TC-1, TC-Thio, and TC-Py. Decreased % growth is visualised as orange while increases are shown as blue. **b** Cytotoxicity screening of Cu complexes against cell lines with varied intracellular Cu levels, with 48 h incubation and using 3× $CuCl_2$ as a control.

https://doi.org/10.1038/s41467-026-68911-5

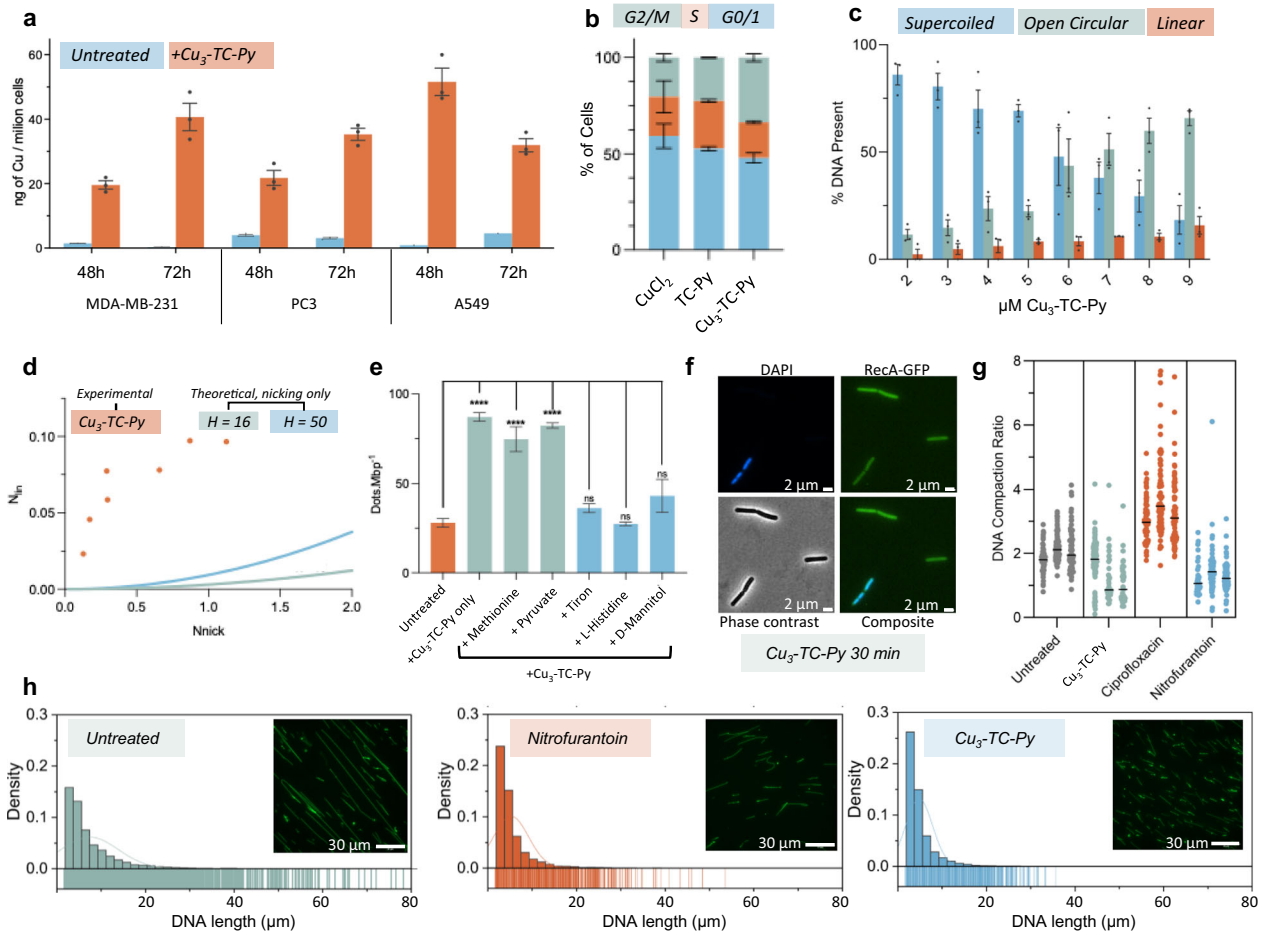

Fig. 4 | DNA damaging experiments. a ICP-MS measurements of intracellular Cu localisation in MDA-MB-231, PC3 and A549 cells after exposure to 10 μM of Cu_3-TC-Py for 48 (blue) and 72 h (orange). Data are presented as mean ± SEM. **b** Cell cycle analysis showing phase distribution in treated and untreated MDA-MB-231 cells. Data are presented as mean ± SEM. **c** Band densitometry analysis obtained from pUC19 cleavage experiments with Cu_3-TC-Py. Data are presented as mean ± SEM. **d** Freifelder-Trumbo analysis of the Cu_3-TC-Py cleavage profile. Blue and green plots are theoretical plots for nicking-only agents where H (the number of base pairs within which two nicking events occur) is set to 16 or 50 bp. Orange dots represent values calculated from densitometry values. **e** RADD experiments with peripheral blood monoclonal cells (PBMCs). Untreated represents the density of lesions observed in untreated PBMCs, control is that in cells treated with Cu_3-TC-Py only. All other bars are indicative of samples treated with Cu_3-TC-Py where the indicated antioxidant was prophylactically incubated with PBMCs. Data are presented as mean ± SEM. Statistical analysis was performed using one-way ANOVA with Tukey's multiple comparisons test in GraphPad Prism. All statistical tests were two-sided. *P* values are indicated as follows: $P < 0.05$ (*), $P < 0.01$ (**), $P < 0.001$ (***), $P < 0.0001$ (****); n.s., not significant ($P \geq 0.05$). P values were as follows; untreaded vs +Cu_3-TC-Py only ($P < 0.0001$), untreated vs +Cu_3-TC-Py and methionine ($P < 0.0001$), untreated vs +Cu_3-TC-Py and pyruvate ($P < 0.0001$) untreated vs +Cu_3-TC-Py and tiron ($P = 0.8454$), untreated vs +Cu_3-TC-Py and L-histidine ($P > 0.999$), untreated vs +Cu_3-TC-Py and D-mannitol ($P = 0.2168$). **f** Microscopy images of *Bacillus subtilis* treated with 750 μM Cu_3-TC-Py for 10- and 30-min. Composite image is an overlay of DAPI and RecA-GFP images. Scale bars indicate 2 μm (**g**) DNA compaction ratio analysis where *B. subtilis* was treated with 750 μM of Cu_3-TC-Py, 3 μM ciprofloxacin, or 268 μM nitrofurantoin for 30 min. Individual values represented as dots, mean values shown as black lines. Triplicate experiments are shown as individual groups within the sample group plot (**h**) Single-molecule profile analysis of DNA extracted from *B. subtilis* along with cells treated with nitrofurantoin or Cu_3-TC-Py. Inset images are representative microscope images from each experiment. Scale bars indicate 30 μm.

The Freifelder-Trumbo model (Eqs. 1–3) correlates the number of single strand nicks (n_{nick}) and the number of linearisation events (n_{lin}) per plasmid molecule in each sample based on the relative presence of the three forms. A plot of n_{lin} versus n_{nick} can then be compared to the theoretical nicking only plot to identify independent DSB formation. The value of H in this model represents the minimum number of base pairs within which two nicking events must occur for the plasmid to revert to its linear form. This parameter has been a subject of some debate, with calculated values ranging from 16 to 50 base pairs[39]. To ensure that any deviation from the theoretical plots was genuinely indicative of DSBs we calculated theoretical plots with H values of 16 and 50. The plot of n_{lin} versus n_{nick} for Cu_3-TC-Py in Fig. 4d significantly departs from both theoretical plots and strongly indicates that the complex cleaves DNA through a combination of nicking and independent DSBs, with the former predominating.

$$F_{linear} = n_{lin} e^{-n_{lin}} \quad (1)$$

$$F_{supercoiled} = e^{-(n_{nick} + n_{lin})} \quad (2)$$

$$n_{lin} = \frac{n_{nick}^2 (2H+1)}{4L} \quad (3)$$

To probe the cleavage mechanism, experiments in the presence of non-covalent DNA binding agents and antioxidants were undertaken (Supplementary Fig. 33)[40,41]. First, the presence of major groove binding methyl green (MG) produced a significant increase in damage while activity was completely inhibited by netropsin—a known minor

groove binding agent. Next, antioxidant experiments revealed that cleavage was maximally inhibited by tiron, a superoxide scavenger, and N,N-dimethyl thiourea (DMTU), a peroxide scavenger. Taken together these results indicate Cu_3-TC-Py mediates oxidative DNA cleavage within the minor groove using a Fenton / Haber-Weiss type catalytic cycle and further supports the minor groove binding preference identified in earlier fluorescence melting experiments.

Repair-assisted damage detection

We next assessed the ability of Cu_3-TC-Py to induce intracellular DNA damage using a single-molecule repair-assisted damage detection (RADD) protocol (Fig. 4e)[42]. Here, peripheral blood monoclonal cells (PBMCs) were treated with Cu_3-TC-Py or left untreated. In parallel PBMCs were pre-treated with a range of antioxidants prior to Cu_3-TC-Py treatment. Genomic DNA was extracted from the cells and incubated with DNA repair enzymes. Next, fluorescently labelled deoxynucleotide triphosphate (dNTP) aminoallyl-dUTP-ATTO-647N was added along with a processive DNA polymerase, and the mixture was counterstained with YOYO-1. Finally, individual DNA molecules stretched on functionalised coverslips were imaged using fluorescence microscopy. Individual RADD events were then quantified due to the appearance of red foci arising from the incorporation of ATTO-647N labelled dNTPs. We conducted experiments with a DNA repair cocktail (APE1, Endo III, Endo IV, Endo VIII, Fpg, and AAG). Both Endo IV and APE I were employed to maximise recognition of abasic and oxidised abasic lesions. APE I preferentially cleaves canonical apurinic/apyrimidinic sites within duplex DNA, whereas Endo IV also recognises oxidised and structurally distorted abasic sites and removes 3′ blocking groups. Their combined use therefore broadens detection sensitivity toward the diverse oxidative lesions generated by copper redox cycling. Cu_3-TC-Py treatment alone generated a significant increase in the number of DNA lesions relative to the untreated sample, confirming the ability of the complex to access and damage intracellular genomic DNA. Pre-treatment of the PBMCs with antioxidants, tiron, *L*-histidine, and *D*-mannitol, reduced the observed number of lesions to the same level as the untreated sample, implicating superoxide, singlet oxygen, and hydroxyl radicals, respectively, in lesion formation. Additionally, we found that sodium pyruvate, and *L*-methionine had little effect on the number of lesions observed, suggesting peroxide and hypochlorous acid are not involved in the DNA damage mechanism of Cu_3-TC-Py. This data distinguishes Cu_3-TC-Py from earlier Cu_3-TC-1 and Cu_3-TC-Thio complexes which act predominantly via a superoxide- and peroxide-dependent mechanisms.

Cytological profiling in bacterial models

To probe the structural changes imposed on DNA by Cu_3-TC-Py, the AMN activity was examined in bacterial cells using a combination of cytological profiling, using phase contrast microscopy and DAPI DNA staining, functional profiling using GFP-tagged RecA (which is an essential protein for maintaining and repairing DNA in bacteria), and DnaN (the beta subunit of DNA polymerase III), along with single-molecule analysis. We first treated *Bacillus subtilis* with Cu_3-TC-Py for 10 and 30 min before staining and imaging via phase contrast and fluorescence microscopy (Fig. 4f). DNA targeted agents can be expected to cause a change (compaction or relaxation) of the bacterial nucleoid while a DNA damaging agent such as an AMN may be expected to increase recruitment of RecA and trigger a resultant increase in RecA foci. Ciprofloxacin and nitrofurantoin were used as controls in these experiments. Ciprofloxacin inhibits DNA gyrase and topoisomerase IV causing defects in DNA replication and nucleoid separation resulting in clear nucleoid compaction and recruitment of the RecA protein to single-stranded DNA arising from strand breaks. Nitrofurantoin is a prodrug that is activated by cellular nitroreductases leading to the formation of reactive species that damage cellular macromolecules, most prominently DNA, causing nucleoid relaxation and, at high doses, destruction of the entire nucleoid. Relative to the positive controls treated with ciprofloxacin and nitrofurantoin, Cu_3-TC-Py resulted in an apparent loss of DAPI staining together with limited recruitment of GFP-RecA foci (Supplementary Figs. 34, 35). Given the earlier evidence of combined AMN and DNA condensation activity by Cu_3-TC-Py, we hypothesised this cytological profile may arise due to near-total degradation of the genetic material. Therefore, we conducted image analysis to identify the DNA compaction ratio within imaged cells (Fig. 4g) where the compaction ratio is an expression of the nucleoid volume relative to the total cell volume. Theoretically, DNA degradation causes a decrease in the DNA compaction ratio as the nucleoid is dispersed, while compaction would have the inverse effect. Data here showed that after 30 min, Cu_3-TC-Py significantly decreased the DNA compaction ratio, producing a similar profile to nitrofurantoin, thus demonstrating Cu_3-TC-Py damages and disperses the genetic material. It should be noted that nitrofurantoin followed a slower kinetic profile, characterized by RecA foci appearing at 10 min, followed by nucleoid relaxation, loss of DAPI signal, and loss of RecA foci at 30 min, while Cu_3-TC-Pyr already showed DNA dispersal at 10 min (Supplementary Fig. 36). This faster effect explains the absence of a high number of RecA foci in Cu_3-TC-Pyr treated samples as RecA cannot form filaments when the nucleoid is physically disintegrated. Since Cu_3-TC-Pyr showed preferential binding to the minor groove, which is also the binding site of DAPI, the lower signal intensity could be attributed to competition for this binding site. However, competitive binding would not explain the absence of RecA foci as the localisation of DNA-binding proteins is not affected by DAPI staining. Indeed, the DNA-binding DNA polymerase III subunit, DnaN, localises in the expected nucleoid-associated foci in untreated but DAPI-stained cells, but is dispersed after treatment with Cu_3-TC-Py (Supplementary Figs. 37, 38)[43]. Since a loss of DAPI signal is also observed with nitrofurantoin, which does not bind to DNA but disperses the nucleoid in a similar manner as Cu_3-TC-Py, nucleoid fragmentation is a considerably more likely explanation for the dispersed DAPI signal and the loss of protein localisation than competition between DAPI and Cu_3-TC-Py for the minor groove, although it cannot be excluded that the latter may partially contribute to the reduced DAPI signal.

Independent confirmation of this nucleoid-degrading mechanism was then sought using a combination of gel electrophoresis and single-molecule analysis, choosing the 30 min timepoint at which both Cu_3-TC-Pyr and nitrofurantoin showed nucleoid dispersal. Gel electrophoresis experiments involved treating cells in an identical manner to those used for the image analysis presented in Fig. 4f. Thereafter, the total DNA content was extracted and visualised using pulse-field agarose gel electrophoresis where changes in DNA molecule sizes are clearly identifiable. Untreated samples contained relatively uniform DNA molecules while those treated with Cu_3-TC-Py demonstrated reduced overall DNA content together with fragmentation patterns indicative of DNA ablation (Supplementary Fig. 39). Tandem single-molecule analysis experiments were then performed using the same treatment and extraction steps. Here, DNA was stained using YOYO-1, stretched on cover slides and imaged (Fig. 4h). Shortening of DNA molecules was evident as untreated samples contained high counts of molecules in the 40-80 μm range, while samples treated with Cu_3-TC-Py and nitrofurantoin contained limited numbers of molecules above 40 μm and a significantly increased density of molecules below 20 μm.

Discussion

Click chemistry, including the copper(I)-catalysed azide-alkyne cycloaddition (CuAAC) reaction, is a staple of modern synthetic chemistry and continues to provide functionality to new fields. Here, we applied the CuAAC reaction to diversify and expand the DNA damaging potential of new polynuclear copper metallodrug candidates. Six new ligands of the Tri-Click (TC) class were prepared and their ability to coordinate three copper(II) ions was determined using

electrospray ionisation-mass spectrometry (ESI-MS). Data show that N,N-donor systems of TC-Py (Pyridine), TC-Pyrm (Prymidine), and TC-Benzo (Benzothiazole) form trinuclear complexes, while N,O- systems such as TC-OH (Hydroxide) and TC-Acid (Carboxylic acid) produce mixtures of complexes with varying nuclearity. Competitive fluorescence displacement experiments indicate that the N,N-complexes Cu_3-TC-Py and Cu_3-TC-Pyrm possess exceptionally high DNA recognition properties, surpassing earlier reported TC-1 and TC-Thio complexes[14,15]. Next, fluorescence quenching probes revealed preferential minor groove binding with the N,N-donor complexes outperforming other agents in this screen. Competition and quenching data were combined to select Cu_3-TC-Py as the leading candidate, and to better understand its DNA recognition mode, advanced analysis involving microscale thermophoresis (MST), Förster resonance energy transfer (FRET) melting, and single-molecule DNA imaging experiments were performed. These techniques revealed a bi-phasic interaction mode consisting of high-affinity DNA binding characterised by stabilisation of duplex DNA, followed by molecular condensation associated with charge neutralisation. In-depth FRET melting experiments with diverse DNA hairpins further demonstrated the minor groove specificity of Cu_3-TC-Py and also revealed a marked preference for GC-rich DNA. In-silico docking and molecular dynamics corroborate the complex preferentially binding within the minor groove across a six-base pair binding site with binding predominantly stabilised by electrostatic forces augmented by van der Waals interactions that are otherwise lacking when the complex resides in the major groove.

Broad-spectrum NCI-60 screening of TC-Py and TC-Thio identified both ligands had promising activity against a range of human cancer cell lines including MDA-MB-231. This result contrasts with the earlier reported TC-1 scaffold and supports the role of heteroaromatic groups in promoting cytotoxicity. Cytotoxicity screening of Cu_3-TC-Py and Cu_3-TC-Thio showed Cu_3-TC-Py to be a substantially more potent agent with a clear ability to internalise intracellular Cu ions when monitored via ICP-MS. Differences here may arise from the persistent bidentate coordination around each copper centre in TC-Py, in contrast to TC-Thio, which was found to chelate copper(I) only. Favourable NCI-60 and ICP-MS indications prompted our investigation into the DNA damaging properties of Cu_3-TC-Py on native DNA and within cellular models. Firstly, native DNA damaging studies showed Cu_3-TC-Py cleaves pUC19 through a mixture of single and double strand breaks with high efficiency compared to other copper AMN systems[17]. The intracellular DNA damage repair response triggered by Cu_3-TC-Py was then probed using single-molecule DNA imaging of primary blood monoclonal cells (PBMCs). Here, DNA lesions characteristic of oxidised purine and pyrimidine bases were identified with further analysis revealing intracellular ROS associated with superoxide, singlet oxygen, and hydroxyl radicals chiefly mediate lesion formation. To investigate these effects further, functional assays revealed that Cu_3-TC-Py disrupts normal DNA packing in bacterial cells, resulting in DNA dispersion.

The discovery of Cu_3-TC-Py from the broader series demonstrates the use of click chemistry in metallodrug discovery and points to a conserved set of structural features adapted to maximise artificial metallo-nuclease activity. While the TC scaffold serves as a strong foundation for designing DNA-damaging candidates, advancing TC-Py to the clinic will require investigation into its in vivo biological stability when complexed with bioavailable copper. Given recent developments in the study of metallothionein and its impediment of oxygen activators[44], the strategic inclusion of pyridine donor groups within the TC scaffold may enhance intracellular stability and improve clinical viability.

Method

Work presented here complies with all relevant ethical regulations. The use of blood samples was approved by the Regional Ethical Review Board in Gothenburg (Dnr: 246-07 and Dnr: 308-08). Chemicals and reagents were sourced from Sigma-Aldrich and Tokyo Chemical Industry (TCI) and were used without any further purification. HPLC grade chloroform and methanol were used without further purification. ^{1}H and ^{13}C NMR spectra were obtained on a Bruker AC 600 MHz NMR spectrometer and processed in MNova (MastreLab). Thermal melting analysis was performed on a Roche LightCycler 480 II. Fluorescence quenching assays were performed using commercial EtBr, Hoechst 34580 (Sigma) and Methyl green (TCI) and plates were read on a TECAN Spark® microplate reader. Microscale thermophoresis experiments were conducted on a Nanotemper Monolith® instrument using standard capillaries. Human topoisomerase I was acquired from Sigma.

Synthesis

TC Ligands were prepared using the copper catalysed alkyne-azide cycloaddition (CuAAC) of 2,4,6-Tris-(azidomethyl)-mesitylene (Triazide) with a variety of commercially available alkynes in the presence of the co-catalyst tris-hydroxypropyltriazolylmethylamine (THPTA). In all cases the aqueous solutions of active catalyst was prepared in situ by dissolving appropriate quantities of Cu(II) sulphate (1 mol %) and THPTA (1 mol %) in 0.5 mL of water followed by addition of 0.5 mL aqueous Na-*L*-ascorbate (5 mol %).

2,4,6-Tris-(azidomethyl)-mesitylene (triazide): To a solution of 2,4,6-tris-(bromomethyl)-mesitylene (1.025 g, 2.56 mmol) in acetone (50 mL) sodium azide (1.00 g, 15.38 mmol) was added in portions over ice over a period of 20 min. (Caution! Sodium azide is acutely toxic and is an explosion hazard. Refer to organic azide stability guidelines prior to the preparation of any azide compounds). The reaction was refluxed overnight and allowed to cool to room temperature. The suspension was gravity filtered and the filtrate was dried under reduced pressure to yield the title product as a crystalline white solid. NMR data was in line with previously reported results.

(((2,4,6-trimethylbenzene-1,3,5-triyl)tris(methylene))tris(1H-1,2,3-triazole-1,4-diyl))trimethanol (TC-OH): The active catalyst solution was added to a solution of triazide (100 mg, 0.35 mmol) in DMF (5 mL) and allowed to stir for 10 min. The resulting solution was then added dropwise to a stirring solution of propargyl alcohol (196 mg, 3.5 mmol) in DMF (5 mL). The flask was flushed with nitrogen and allowed to stir overnight at room temperature. The bright yellow solution was dried under a stream of nitrogen. The yellow solid was suspended in acetone (5 mL) with sonication. The title product (125 mg, 81%) was isolated by vacuum filtration and washing with ice cold acetone (5 × 5 mL). ^{1}H NMR (DMSO, 600 MHz): δ 2.42 (s, 9H) 4.48 (d, 6H, J = 5.5 Hz) 5.13 (t, 3H, J = 5.5 Hz) 5.66 (s, 6H) 7.76 (s, 3H). ^{13}C NMR (DMSO, 151 MHz) δ: 16.78, 48.73, 55.45, 122.80, 131.42, 139.64, 148.36. ESI-MS positive ionization mode: $[M + H]^+$ Calculated m/z = 454.23 found m/z = 454.23, [M+Na] calculated m/z = 476.21 found m/z = 476.21.

1,1′,1″-((2,4,6-trimethylbenzene-1,3,5-triyl)tris(methylene))tris(1H-1,2,3-triazole-4-carboxylic acid) (TC-Acid): The active catalyst solution was added a solution of triazide (100 mg, 0.35 mmol) in methanol (10 mL) and stirred at room temperature for 10 min. The resulting solution was added dropwise to a solution of propiolic acid (98 mg, 1.4 mmol) in methanol (5 mL). The reaction flask was flushed with nitrogen, sealed and the reaction was stirred vigorously overnight. A white precipitate was removed by vacuum filtration. The filtrate was dried under reduced pressure to yield a white solid that was then suspended in acetone (5 mL) with sonitcation and isolated by decanting. The remaining solid was dried over desicant to yield the title product as a white solid. Yield = 145 mg (83 %). ^{1}H NMR (DMSO 600 MHz): δ 2.38 (s, 9H), 7.74 (s, 6H) 8.55 (s, 3H) 13.14 (s, 3H) ESI-MS (negative ionization mode): ESI-MS negative ionization mode: $[M + H]^+$ calcualted m/z = 496.17 found m/z = 496.17. $[M+Na]^+$ calculated m/z = 518.15 found m/z = 518.15.

1,1′,1″-((2,4,6-trimethylbenzene-1,3,5-triyl)tris(methylene))tris(1H-1,2,3-triazole-4-carboxamide) (TC-Amide): The active catalyst solution

was added a solution of triazide (159.2 mg, 0.56 mmol) in degassed ACN (8 mL). The mixture was allowed to stir for 15 minutes before the dropwise addition of propiolamide (115 mg, 1.67 mmol). The reaction mixture was allowed to stir at room temperature for 3 hours. The title product was collected by vacuum filtration washed with cold acetonitrile (3 ×5 mL) and dried over desiccant. yield = 270 mg (98 %). ^{1}H NMR (DMSO, 600 MHz): δ 2.38 (s, 9H), 5.74 (s, 6H), 8.34 (s, 3H). ESI-MS: $[M+Na]^+$ m/z calculated = 515.20 found m/z = 515.20.

2,2′,2″-(((2,4,6-trimethylbenzene-1,3,5-triyl)tris(methylene)) tris(1H-1,2,3-triazole-1,4-diyl))tripyrimidine (TC-Pyrm): The active catalyst solution was added to a stirring solution of triazide (91 mg, 0.32 mmol) in methanol (8 mL). The mixture was allowed to stir at room temperature for 15 min before dropwise addition of 2-ethynyl pyrimidine (100 mg, 0.96 mmol) in methanol (1 mL). The title product was isolated as a off-white solid by vacuum filtration, washing with 5 mL 0.1 M aqueous EDTA solution and 5 mL acetone. Yield = 170 mg, 89%.^{1}H NMR (DMSO, 600 MHz): δ 2.48 (s, 9H), 5.76 (s, 6H), 7.42 (t, 3H J = 4.96 Hz) 8.57 (s, 3H), 8.83 (d, 6H, J = 4.88 Hz). ESI-MS: $[M + H]^+$ calculated m/z = 598.327 found m/z = 598.26 $[M+Na]^+$ calculated mz/ = 620.25 found m/z = 620.25.

2,2′,2″-(((2,4,6-trimethylbenzene-1,3,5-triyl)tris(methylene)) tris(1H-1,2,3-triazole-1,4-diyl))tripyridine (TC-Py): An activated catalyst solution consisting of 1 mol% CuSO4 and 5 mol% Na-L-Ascorbate was added to a stirring solution of triazide (120 mg, 0.42 mmol) in methanol (8 mL). The mixture was allowed to stir at room temperature for 15 minutes before dropwise addition of 2-ethynyl pyridine (132 mg, 1.28 mmol) in methanol (2 mL). The reaction mixture was allowed to stir for 16 h at room temperature. The title product was isolated as a white solid by vacuum filtration and washing with 5 mL 0.1 M aqueous EDTA solution, 5 mL acetone and 20 mL Et_2O. Yield = 225 mg, 90%. ^{1}H NMR (DMSO, 600 MHz): δ 2.48 (s, 9H), 2.53 (s, 6H), 7.32 (m, 3H) 7.87 (td, 3H, J1 = 7.4 Hz, J2 = 1.4 Hz) 7.99 (dt, 3H, J1 = 7.94 Hz, J2 = 0.84 Hz) 8.38 (s, 3H) 8.54 (m, 3H). ESI-MS: Found $[M + H]^+$ m/z = 595.28 calculated $[M + H]^{xf}$ = 595.28.

2,2′,2″-(((2,4,6-trimethylbenzene-1,3,5-triyl)tris(methylene)) tris(1H-1,2,3-triazole-1,4-diyl))tris(benzo[d]thiazole) (TC-Benzo): To a stirring solution of triazide (119 mg, 0.4 mmol) in methanol (20 mL), were added solutions of CuSO4 (5 mol%) and (+)-Sodium L-ascorbate (20 mol %) in water (0.5 ml each). The mixture was allowed to stir for 15 min before being added dropwise to a solution of 2-ethynyl benzothiazole (200 mg, 1.2 mmol) in methanol (5 mL). The flask was flushed with nitrogen, sealed, and allowed to stir overnight at room temperature. A yellow precipitate formed. The reaction volume was reduced to 3 mL and the title product collected by vacuum filtration (310 mg, 99%). ^{1}H NMR (DMSO, 600 MHz): δ 5.85 (s, 6H), 7.45 (t, 3H, J = 7.41 Hz), 7,52 (t, 3H, J = 8.19 Hz), 7.97 (d, 3H, J = 7.73 Hz), 8.14 (d, J = 7.41 Hz), 8.79 (s, 3H) ESI-MS: [M + H]+ calculated = 763.20 found m/z = 763.19 [M+Na]+ calculated m/z = 785.18 found m/z = 785.18.

Crystallography

The data were collected at 100(1)K on a Synergy, Dualflex, AtlasS2 diffractometer using CuKα radiation (λ = 1.54184 Å) and the CrysAlis PRO suite[45]. Using shelXle[46] and Olex2[47] the structure was solved by dual space methods (SHELXT[48]) and refined on F^2 using all the reflections (SHELXL-2019/2[49]). All the non-hydrogen atoms were refined using anisotropic atomic displacement parameters and hydrogen atoms were inserted at calculated positions using a riding model. Crystal parameters, data collection and structure refinement details are summarised in Supplementary Fig. 1 and Table 2.

Verification of in-situ complexation by ESI-MS

Formation of TC-Cu_3 complexes in-situ was investigated using ESI-MS. Solutions of TC ligands were prepared in DMF prior to addition of three equivalents of aqueous Copper(II) nitrate trihydrate. Samples were vortexed and incubated at 37 °C for 30 min before further dilution (as required) and analysis on a MaXis HD quadrupole electrospray time-of-flight (ESIQTOF) mass spectrometer (Bruker Daltonik GmbH, Bremen, Germany), using a glass syringe (Hamilton) and syringe pump (KD Scientific, Model 781100) for infusions at a flow rate of 3 mL/min.

Verification of in-situ Cu_3-TC-Py complexation by UV-Vis spectroscopy

100 μM TC-Py was prepared in DMSO and added to a 100 μL Quartz cuvette. $Cu(NO_3)_2$ was added as a solution in DMSO such that each addition increased sample concertation by 25 μM (0.2 μL of 12.5 mM). Samples were mixed thoroughly and allowed to stand for ten minutes before recording UV-Vis spectra from 270–800 nm. Absorbance at 283 nm (A_{283}) was recorded and values corrected for dilution factors. A_{283} was then plotted vs the equivalents of $Cu(NO_3)_2$ to TC-Py. The resulting plot was split into two linear sections and fit using the intersecting lines in GraphPad Prism to find the crossing point.

Fluorescence Quenching

Competitive ethidium bromide displacement was conducted as previously reported with slight modification[50]. Briefly, a triplicate serial dilution of test compound was prepared on a 96 well plate to a volume of 50 μL. 50 μL of a working solution of EtBr (25.2 μM) and ctDNA (25 μM) was then added to give a final volume of 100 μL, 12.5 μM EtBr, 12.5 μM ctDNA. All solutions were prepared in 80 mM HEPES, 25 mM NaCl, 5% DMSO. Control wells contained EtBr and ctDNA at equivalent concentration to the test. Blank wells contained EtBr only in the same buffer. Fluorescence intensity due to DNA / EtBr binding was calculated using Eq. 4.

$$F = (F_s - F_b)/(F_c - F_b) \quad (4)$$

Where F is the (fractional) normalised intensity of fluorescence due DNA-bound EtBr. F_s is the observed fluorescence of the sample well, F_b is the fluorescence of the blank well and F_c is the fluorescence observed in the control well. Experiments conducted with Hoechst 34580 and Methyl green were conducted under equivalent conditions but with 5 μM fluorophore. Data was collected on a TECAN® Spark microplate reader. Fluorescence quenching of methyl Green and Hoechst 34580 were conducted in an equivalent manner but with final fluorophore concentrations of 5 μM. Excitation emission wavelengths used were 530/590 nm for EtBr, 350/450 nm for Hoescht 34580 and 630/670 nm for MG.

Microscale Thermophoresis

Samples for MST analysis were prepared to contain 500 nM F-DDH in 80 mM HEPES, 25 mM NaCl, 5% DMSO with Cu(II)-TC-Py at varying concentrations. MST power was set to medium and excitation power was set to automatic mode in the red channel, typical excitation power was approximately 14%. The laser-on time was set to 20 s and with data being recorded for two seconds prior to the laser being turned on and for 2 s post being turned off.

Fluorescence Melting

Thermal melting analysis was performed on a Roche LightCycler®480 II using 80 mM HEPES 25 mM NaCl buffer. Prior to analysis DNA hairpins were denatured by heating to 90 °C (10 °C/min, 2 min hold) and reannealed at 12 °C (0.5 °C/min, 20 min hold). Sample tubes for analysis were prepared to contain 1 μM FRET-labelled hairpins and Cu_3-TC-Py at various concentrations prepared via serial dilution. Melting was conducted in triplicate at a ramp rate of 0.5 °C min^{-1} up to a maximum of 95 °C. Tm values were taken as the midpoint of the melting curves, found from the peak of the first derivative.

Single molecule analysis—DNA binding

Samples for analysis were prepared to contain 5 μM (base pairs) of λ-DNA and 5 μM YOYO-1 with varied concentrations of Cu(II)-TC-Py in a total volume of 10 μL and incubated for 30 min at room temperature. Before imaging, 0.5 μL of β-mercapto ethanol was added to minimize YOYO-1 photocleavage and the sample was diluted to 50 μL to prevent overloading of nanochannels. Samples were added to nanofluidic chips that were fabricated as described elsewhere[51,52]. Compressed air was used to move DNA molecules from the sample well, into the microchannel and to accumulate at the nanochannel interface. Air pressure was then increased manually to drive DNA molecules into nanochannels where images were taken at the excitation and emission wavelengths of YOYO-1 with 2% excitation laser intensity, collecting 20 frames at 100 ms exposure times each to give 2 s videos of each imaging field.

Data analysis was performed with the freeware ImageJ and a custom-written MatLab based software. For DNA confined in nanochannels a kymograph (timetrace) was extracted for each movie using ImageJ and the average distance between either end of the DNA molecule and the average pixel intensity along the DNA molecule was found using the custom MatLab software. For mapping, the initial alignment is done on the center of the molecule to eliminate the effects of drift along the nanochannel. The intensity profile from the molecule is fitted to a linear combination of error functions. A finer alignment procedure is subsequently performed on distinct features (peaks or dips in intensity) along the DNA.

Docking studies

Docking studies of Cu(II)-TC-Py with a B-DNA dodecamer (PDB: 1BNA) was performed using AutoDock Vina[53]. The Cu(II)-TC-Py was prepared by first removing nitrates from the DFT structure. Atomic charges and rotatable bonds were then defined in Autodock tools (version 1.5.7) and the structure output file saved in.pdbqt format. The DNA receptor was prepared by removing water molecules, building in missing hydrogen atoms, and assigning atomic charges. Grid boxes were sized to incorporate the entire DNA fragment and 10 docking poses were tested and ranked in terms of stability using the scoring function in AutoDock Vina.

Molecular dynamics

MD simulations were performed using the GROMACS-2018.4 code[54,55]. The topology and parameters for the DNA model were defined by the CHARMM36m classical mechanics force field[56]. The topology and parameters for Cu(II)-TC-Py were obtained from density functional theory (DFT) calculations using the Gaussian 16 package followed by CHARMM-compatible charge fitting with Antechamber7 using Restrained Electrostatic Potential (RESP) calculations[57].

The Cu(II)-TC-Py–DNA complex was solvated in a large cuboid of TIP3P water molecules with counterions added to balance any formal charge. 0.15 M NaCl was added to model physiological salt concentration. The force field and water model were chosen for its established accuracy in describing metal–DNA interactions and hydration effects within the minor and major grooves. Energy minimisation was followed by thermalisation and equilibration under constant volume (NVT) and then constant pressure (NPT) conditions. Production MD simulations were carried out for 4 μs for each complex, starting with PCU in the minor groove or PCU in the major groove, for a total of 8 μs of free dynamics, sufficient to capture local Cu(II) coordination dynamics and base-pair conformational fluctuations without the need for enhanced sampling techniques. Summary of the simulation setup is provided in Supplementary Table 1.

Characterisation of interactions

We performed the characterisation of interactions in Cu_3-TC-Py -DNA complexes by using the protein–ligand interaction profiler (PLIP)[58], a web service for visualization and detection of non-covalent (hydrogen bonds, metal complexes, hydrophobic interactions, stacking and salt bridge) binary contacts in 3D complex structures. The analysis was carried out in two parts: first, for the full 4 μs trajectory of each system accounting for frames every 100 ns, and second, for the last 1 μs of converged trajectory accounting for frames every 1 ns.

National Cancer Institute 60 cell line screening (NCI-60)

TC-1 (NSC: 843989), TC-Thio (NSC: 843990), and TC-Py (NSC: 843991) were submitted to the U.S. National Cancer Institute (NCI) Developmental Therapeutics Program (DTP) for 60 human cancer cell line screening. Growth inhibition (GI_{50}) data were identified using a five-dose exposure level and are shown in Supplementary Fig. 4. These results are categorised by cancer type across leukaemia, non-small cell lung cancer, colon cancer, CNS cancer, melanoma, ovarian cancer, renal cancer, prostate cancer, and breast cancer and visualised in a heat map using GraphPad Prism as shown in Supplementary Fig. 29.

ICP-MS studies of intracellular Cu

MDAMB231, A549, DU145 and PC3 cells were seeded (700 K for 48 h experiments and 350 K for 72 h experiments) in a 100 mm diameter Petri dish using appropriate medium and incubated at 37 °C, 5% CO_2. When the cell confluency reached 70%, fresh medium containing 10 μM of each complex was added and incubated for an additional 48 h or 72 h at 37 °C, 5% CO_2. Cells were harvested by trypsinization and counted. After centrifugation 300 × *g*, 3 min, cell pellets were washed twice with cold DPBS. To determine the total copper uptake, 2×10^6 cells were collected and digested using 500 μL of 70% nitric acid at 60 °C for 12 h. The acid solution was further diluted 30 times in MilliQ water, and the copper concentration was measured using ICP-MS. Note: the copper(II) source used for all experiments, and controls, was copper(II) chloride.

Anticancer screening of Cu-TC complexes

Cells were seeded at 6000 cells/well density for A549, MDAMB231 and DU145 and 8000 cell/well for PC3, in 96-well plates (100 μL/well) and were incubated at 37 °C, 5% CO_2 for 48 h in DMEM-F12 medium for MDAMB231 cells, in F12K medium for A549 and PC3 cells and in RPMI medium for DU145 cells. Mediums were completed with 10% Foetal bovin serum and 1% penicillin streptomycin (100 U/ml). The medium was replaced by test compound dilutions in fresh medium (100 μL/well) and cells were incubated at 37 °C, 5% CO_2 for 48 h in DMEM-F12 medium for MDAMB231 cells, in F12K medium for A549 and PC3 cells and in RPMI medium for DU145 cells. Mediums were completed with 10% Foetal bovin serum and 1% penicillin streptomycin (100 U/ml). The medium was replaced by test compound dilutions in fresh medium (100 μL/well) and cells were incubated at 37 °C, 5% CO_2 for 48 h. After 44 h, the medium was replaced with 100 μL of fresh medium containing resazurin (0.2 mg/mL). After 4 h of incubation at 37 °C, 5% CO_2, plates were read using a citation 5 Microplate Reader (λ_{exc} = 540 nm; λ_{read} = 590 nm). Fluorescence data were normalized, then they were fitted using GraphPad Prism Software and IC_{50} was calculated by non-linear regression.

Cell cycle analyses

Cell cycle analysis was carried out using the Click-iT EdU Cell Proliferation Assay Kit (ThermoFisher Scientific) according to the manufacturer's instructions. Briefly, the MDA-MB-231 cells were seeded and treated as described above for 48 h. EdU was pulsed for 2 h before cell harvest and subsequent flow cytometry analysis. Cell cycle data were analyzed using BD CSampler Plus software according to the gating strategy provided by the kit.

Bacterial assays

Bacterial growth conditions and compounds preparation: Unless stated otherwise, *Bacillus subtilis* strains were aerobically grown in Mueller Hinton Broth (MHB). All tested compounds except for ciprofloxacin were dissolved and diluted in DMSO. Ciprofloxacin was dissolved and diluted in water. Unless stated otherwise, all assays were performed in biological triplicates. Minimal inhibitory concentrations (MICs) were

determined in a broth microdilution assay according to Clinical and Laboratory Standards Institute (CLSI) guidelines. The MIC was defined as the lowest concentration inhibiting growth of a 5×10^5 colony forming units (CFU)/mL inoculum after a 16-h incubation period at 37 °C.

Bacterial cytological profiling (BCP): Bacterial cytological profiling was performed as described by Wenzel et al.[15]. In short, *B. subtilis* UG10[16] (*trpC2 amyE::Pxyl-recA-mgfp*) was grown in Muller Hinton Broth (MHB) supplemented with 0.1% (w/v) xylose at 30 °C. After reaching an OD_{600} of 0.3, cells were treated with 0.5× and 1× MIC of the respective compounds for 10- and 30-min. Ciprofloxacin and nitrofurantoin were used as positive controls. Immediately prior to imaging, cells were stained with 1 μg/mL of the DNA dye DAPI for 5 min. Samples (0.5 μL) were spotted on glass slides covered with a thin film of 1.2% agarose, covered with a poly-L-dopamine-coated coverslip[17], and imaged using a Nikon Eclipse Ti2 inverted fluorescence microscope equipped with a CFI Plan Apochromat objective (DM Lambda 100X Oil N.A. 1.45, W.D. 0.13 mm, Ph3), a Lumencor Sola SE II FISH 365 light source, a Photometrics PRIME BSI camera, an Okolab incubator, and Nis ELEMENTS AR 5.21.03 software.

BCP image analysis: Images were processed and analyzed with Fiji and the ImageJ plugin MicrobeJ[18,19]. The MicrobeJ parameters for bacterial detection in the phase contrast were set to smoothed segmentation with an area of 1 μm^2-max. The width and circularity were adjusted accordingly to ensure proper detection while other parameters remained at default settings. All chained cells were assessed and separated using the MicrobeJ manual editing interface[19]. For DNA compaction analysis, the maxima of foci detection were used as described previously[20]. The parameters within the maxima detection remained at default settings. The Z-score and tolerance were adjusted manually to ensure fitting DNA detection. The compaction was calculated based on the quotient of the cell area divided by the DNA area. To quantify RecA-GFP foci, the total number of cells showing the foci and the total number of analysed cells were counted manually. All unfocused and visibly lysed cells were excluded from the analysis. P values were calculated using either heteroscedastic or nested t-tests, as specified in the figure legends, using OriginPro (OriginLab Corporation version 2023) or GraphPad Prism. For the DnaN experiments, *B. subtilis* HM771 (*gfp-dnaN::cat*)[21] was grown in MHB until an OD_{600} of 0.3 and subsequently treated with Cu_3-TC-Py for 25 min. Cells were stained with DAPI for 5 min prior to fluorescence microscopy. Cells were visually examined for the presence or absence of DnaN foci.

Bacterial chromosomal DNA preparation: Overnight cultures of *B. subtilis* 168CA[22] were diluted in 20 mL MHB and grown at 30 °C until reaching an OD_{600} of 0.3. Cells were then split and treated with either 64 μg/mL nitrofurantoin, 0.75 mM AG1, or left untreated as control. After 30 min of treatment, chromosomal DNA was isolated from all samples following a standard phenol-chloroform protocol[23]. DNA was quantified using a Qubit 4 fluorometer following the protocol of the dsDNA Broad Range Assay kit (Invitrogen, Thermo Fisher, USA). Wide bore pipette tips were used throughout the experiment to minimize shear-induced fragmentation of the DNA.

Pulse field gel electrophoresis (PFGE)

Isolated DNA was separated in 20–50 kb resolution by PFGE using a 1% agarose gel run in a CHEF III DR System (Bio-Rad Laboratories, Hercules, CA, United States) with 0.5× TBE (45 mM Tris-HCl, pH 8.0; 45 mM boric acid; 1 mM EDTA) as running buffer. Electrophoresis was performed for 24 h at 14 °C. The forward and reverse voltages were 9 and 6 V/cm, respectively, with an initial switch time of 0.86 s and final switch time of 0.92 s, with a 180° angle. The gel was stained with 1× concentrated SYBR Safe DNA gel stain (Invitrogen) for at least 30 min before imaging in a UV transilluminator with default auto optimal exposure settings for 590/110 SYBR safe gels (BioRad ChemiDoc MP imaging system, ImageLab Touch software v 2.3.0.07).

Bacterial DNA fluorescence microscopy

Silanization of coverslips: Stretching of DNA was performed on silanized glass coverslips. The silanization was done as follows: 18 × 18 mm coverslips were placed in a coverslip rack and carefully submerged in a mixture of 1% (3-aminopropyl)triethoxysilane (Sigma Aldrich) and 1% allyltrimethoxysilane (Sigma Aldrich) in acetone solution, and silanized overnight. The activated coverslips were rinsed with acetone:-water solution (2:1 v/v) and dried under a nitrogen gas flow immediately before DNA stretching.

DNA staining, stretching and imaging

100 ng DNA were stained with 320 nM YOYO-1 (Invitrogen) in 0.5× TBE and supplemented with 2% β-mercaptoethanol (BME, Sigma Aldrich) in a final volume of 50 μL. 3.2 μL of stained DNA sample were placed at the interface of the silanized coverslip and a clean microscopy slide (VWR), causing the capillary force between the silanized coverslip and the microscope slide to stretch the DNA. Extended DNA molecules were visualized using a Zeiss Observer.Z1 fluorescence microscope equipped with an Andor iXON Ultra EMCCD camera and a Colibri 7 LED illumination system. For imaging YOYO-1, band-pass excitation filters (475/40 nm) and band-pass emission filters (530/50 nm) were utilized.

Data analysis*:* A custom-made MATLAB software was used to analyse DNA fragments. Stretched DNA molecules were detected, and the length of each molecule was measured in microns. The software was set to exclude overlapping DNA strands from the analysis. One-way ANOVA statistical significance was determined using Tukey's model for multiple comparisons with a confidence level of 95%. *P* values are represented using the GraphPad PRISM style; $^{****}P < 0.0001$. The distribution graph was created in OriginPro (OriginLab Corporation version 2023).

DNA cleavage by agarose gel electrophoresis

Cleavage reactions were prepared to a final volume of 20 μL in 100 μL Eppendorf tubes and contained 400 ng supercoiled pUC19 DNA, 1 mM Na-L-ascorbate (where indicated) and 25 mM NaCl in 80 mM HEPES buffer (pH = 7.4). Cleavage reactions with ROS scavengers were prepared to contain 10 mM of the ROS scavenger by addition of 1 μL of a 200 mM stock solution prior to DNA addition. Reactions probing the cleavage site were prepared by preparing reaction mixtures to contain 16 μM and 8 μM methyl green and netropsin respectively from stock solutions prepared in 80 mM HEPES buffer (pH = 7.4). Upon addition of pUC19 the samples were incubated for 30 minutes at 37 °C, quenched with 6× loading dye (Thermo Fisher R0611) and loaded on to a 1.3 % agarose gel, prepared using 1× TAE buffer and run at 70 V for 90 minutes.

Repair assisted damage detection

The protocol was adapted from Singh et al.[24,25]. The use of blood samples was approved by the Regional Ethical Review Board in Gothenburg (Dnr: 246-07 and Dnr: 308-08).

Blood Sample Collection: Samples were collected from individuals with normal blood count from the Hematology Lab at the Clinical Chemistry Department at Sahlgrenska University Hospital, Gothenburg, Sweden Lymphoprep (Axis-Shield PoC AS, Oslo, Norway) was used to harvest peripheral blood mononuclear cells (PBMCs) via density gradient-based separation. The blood-based study was performed with mixed blood samples collected from different individuals and pooled together, without consideration of sex/gender.

Treatment of PBMCs with Cu(II)-TC-Py and antioxidants: 5×10^5 PBMCs were treated with 200 μM Cu(II)-TC-Py and incubated for 2 h on a thermal block at 37 °C. For antioxidant-treated samples, PBMCs were pretreated with 1 mM of tiron, L-histidine, L-Methionine, D-mannitol, and sodium pyruvate for 2 h prior to Cu(II)-TC-Py treatment.

Extraction of DNA: DNA was extracted using GenElute-Mammalian Genomic DNA Miniprep Kit (Sigma-Aldrich) following manufacturer's

instructions, after drug treatment and free radical scavenger incubation. DNA concentrations were quantified using a NanoDrop 1000 spectrophotometer. Care was taken to avoid excess shearing of DNA by using wide-bore tips.

Fluorescent labelling of Cu_3-TC-Py induced DNA damage: DNA (100 ng) was incubated with Endo III (2.5 U), Endo IV (2.5 U), Endo VIII (2.5 U), APE1(2.5 U), Fpg (2.5 U) and AAG (2.5 U) in 1× CutSmart Buffer for 1 h at 37 °C for in vitro DNA repair initiation. dNTPs (1 µM of dATP, dGTP, dCTP, 025 µM dTTP and 0.25 µM aminoallyl-dUTP-ATTO-647N) were incorporated at the damage sites in 1× NEBuffer 2 using DNA polymerase I (1.25 U) at 20 °C. Subsequently, the reaction was terminated with 2.5 µl of 0.25 M EDTA.

Silanization of coverslips: 18 × 18 mm glass coverslips (Thermo Fischer Scientific) were placed in a coverslip rack and carefully put into an acetone solution containing 1% (3-aminopropyl) triethoxysilane (APTES) and 1% allyltrimethoxysilane (ATMS) (v/v) and coated overnight[26]. Coated coverslips were rinsed with acetone:water solution (2:1 v/v) to remove residues for reproducible stretching of DNA. The slides were always used on the day they were produced.

Stretching of DNA and imaging: The Aminoallyl-dUTP-ATTO-647N incorporated fluorescent DNA samples were diluted with 0.5× TBE and stained with 320 nM YOYO-1 (Invitrogen) in a total volume of 50 µl. β-mercaptoethanol (2% v/v, Sigma-Aldrich) was added prior to image acquisition to minimize photodamage. The DNA samples were stretched by placing 3.2 µl at the interface of the silane-activated coverslip and a microscopy slide (VWR Frosted). Zeiss Observer.Z1, equipped with an Andor iXON Ultra EMCCD camera and a Colibri 7 LED illumination system was used to obtain the fluorescence images of the stretched DNA molecules. Each image consisted of two colours, YOYO-1 (green channel), and aminoallyl-dUTP-ATTO-647N (red channel) having appropriate band-pass excitation filters (475/40 and 640/30 nm) and bandpass emission filters (530/50 and 690/50 nm).

Software analysis: A custom-made MATLAB script was used to analyse the data which estimates the length of the stretched DNA molecule in micron (µm) and counts the total number of Aminoallyl-dUTP-ATTO-647N dots along the DNA. The results were expressed as Dots.MBp^{-1} by stretching lambda DNA (48502 bp, New England Biolabs) in a similar buffered conditions to determine 1 µm stretched DNA to be ~3000 bp. DNA molecules that overlapped as wells as dots at the end of the DNA molecule which could have resulted from DNA strand breaks during the DNA extraction process were excluded from the analysis.

Statistics: Experiments were performed in technical duplicates and analysed using GraphPad Prism. Statistical significance was assessed using a one-way ANOVA with the assumptions of normal distribution and equal variances. Post-hoc testing was performed using Tukey's multiple-comparisons test. Multiplicity-adjusted p-values are reported using GraphPad Prism notation: ns (not significant), $*P < 0.05$, $**P < 0.01$, $***P < 0.001$, $****P < 0.0001$.

Reporting summary

Further information on research design is available in the Nature Portfolio Reporting Summary linked to this article.

Data availability

All molecular dynamics simulation data supporting the findings of this study, including structure, topology, parameter, and trajectory files for the Cu_3-TC-Py–DNA systems, are publicly available on Zenodo at https://zenodo.org/records/17143195 (DOI: 10.5281/zenodo.17143194). All other data is presented in the supplementary information or the source data file provided. Source data are provided with this paper.

Code availability

The data analysis involving extraction of kymographs from multi-TIFF files and measurement of end-to-end lengths from the obtained kymographs were done using a custom written MATLAB code publicly available on GitHub at https://github.com/dnadevcode/lldev (DOI: 10.5281/zenodo.17652641).

References

1. Kolb, H. C., Finn, M. G. & Sharpless, K. B. Click chemistry: diverse chemical function from a few good reactions. *Angew. Chem. Int. Ed. Engl.* **40**, 2004–2021 (2001).
2. Rostovtsev, V. V., Green, L. G., Fokin, V. V. & Sharpless, K. B. A stepwise Huisgen cycloaddition process: copper(I)-catalyzed regioselective "ligation" of azides and terminal alkynes. *Angew. Chem. Int. Ed. Engl.* **41**, 2596–2599 (2002).
3. Tornøe, C. W., Christensen, C. & Meldal, M. Peptidotriazoles on solid phase: [1,2,3]-triazoles by regiospecific copper(i)-catalyzed 1,3-dipolar cycloadditions of terminal alkynes to azides. *J. Org. Chem.* **67**, 3057–3064 (2002).
4. Meldal, M. & Diness, F. Recent fascinating aspects of the CuAAC click reaction. *Trends Chem.* **2**, 569–584 (2020).
5. Agard, N. J., Prescher, J. A. & Bertozzi, C. R. A strain-promoted [3 + 2] azide–alkyne cycloaddition for covalent modification of biomolecules in living systems. *J. Am. Chem. Soc.* **126**, 15046–15047 (2004).
6. Liang, L. & Astruc, D. The copper(I)-catalyzed alkyne-azide cycloaddition (CuAAC) "click" reaction and its applications. An overview. *Coord. Chem. Rev.* **255**, 2933–2945 (2011).
7. Wang, X., Huang, B., Liu, X. & Zhan, P. Discovery of bioactive molecules from CuAAC click-chemistry-based combinatorial libraries. *Drug Discov. Today* **21**, 118–132 (2016).
8. Hennessy, J. et al. A click chemistry approach to targeted DNA crosslinking with cis-platinum(II)-modified triplex-forming oligonucleotides. *Angew. Chem. Int. Ed. Engl.* **61**, e202110455 (2022).
9. McGorman, B. et al. Enzymatic synthesis of chemical nuclease triplex-forming oligonucleotides with gene-silencing applications. *Nucleic Acids Res.* **50**, 5467–5481 (2022).
10. Hennessy, J. et al. Thiazole orange-carboplatin triplex-forming oligonucleotide (TFO) combination probes enhance targeted DNA crosslinking. *RSC Med. Chem.* **15**, 485–491 (2024).
11. Crowley, J. D. & McMorran, D. A. "Click-Triazole" coordination chemistry: exploiting 1,4-disubstituted-1,2,3-triazoles as ligands. in *Topics in Heterocyclic Chemistry* 31–83 (Springer Berlin Heidelberg, Berlin, 2012).
12. Ahmad, M., Balamurali, M. M. & Chanda, K. Click-derived multifunctional metal complexes for diverse applications. *Chem. Soc. Rev.* https://doi.org/10.1039/d3cs00343d (2023).
13. Mindt, T. L. et al. "Click to chelate": synthesis and installation of metal chelates into biomolecules in a single step. *J. Am. Chem. Soc.* **128**, 15096–15097 (2006).
14. McStay, N. et al. Click and Cut: a click chemistry approach to developing oxidative DNA damaging agents. *Nucleic Acids Res.* **49**, 10289–10308 (2021).
15. Gibney, A. et al. A click chemistry-based artificial metallo-nuclease. *Angew. Chem. Int. Ed. Engl.* **62**, e202305759 (2023).
16. Kellett, A. & McStay, N. Metallodrug therapeutic compounds and prodrugs of metallodrug therapeutic compounds. US Patent Application **US20240376129A1** (2024).
17. Gibney, A. & Kellett, A. Gene editing with artificial DNA scissors. *Chem. Eur. J.* **30**, e202401621 (2024).
18. Chen, J. & Stubbe, J. Bleomycins: towards better therapeutics. *Nat. Rev. Cancer* **5**, 102–112 (2005).
19. Poole, S. et al. Design and in vitro anticancer assessment of a click chemistry-derived dinuclear copper artificial metallo-nuclease. *Nucleic Acids Res.* **53**, gkae1250 (2025).
20. Kellett, A., Molphy, Z., Slator, C., McKee, V. & Farrell, N. P. Molecular methods for assessment of non-covalent metallodrug–DNA interactions. *Chem. Soc. Rev.* **48**, 971–988 (2019).

21. Cheng, Y. & Prusoff, W. H. Relationship between the inhibition constant (K1) and the concentration of inhibitor which causes 50 per cent inhibition (I50) of an enzymatic reaction. *Biochem. Pharmacol.* **22**, 3099–3108 (1973).
22. Jerabek-Willemsen, M. et al. MicroScale thermophoresis: interaction analysis and beyond. *J. Mol. Struct.* **1077**, 101–113 (2014).
23. Jerabek-Willemsen, M., Wienken, C. J., Braun, D., Baaske, P. & Duhr, S. Molecular interaction studies using microscale thermophoresis. *Assay Drug Dev. Technol.* **9**, 342–353 (2011).
24. Seidel, S. A. I. et al. Microscale thermophoresis quantifies biomolecular interactions under previously challenging conditions. *Methods* **59**, 301–315 (2013).
25. Carter, M. T., Rodriguez, M. & Bard, A. J. Voltammetric studies of the interaction of metal chelates with DNA. 2. Tris-chelated complexes of cobalt(III) and iron(II) with 1,10-phenanthroline and 2,2′-bipyridine. *J. Am. Chem. Soc.* **111**, 8901–8911 (1989).
26. Travers, A. Michael Waring-A scientific life in DNA. *Biopolymers* **112**, e23408 (2021).
27. Prieto Otoya, T. D. et al. Probing a major DNA weakness: resolving the groove and sequence selectivity of the diimine complex Λ-[Ru(phen)2 phi]2. *Angew. Chem. Int. Ed Engl.* **63**, e202318863 (2024).
28. Zeglis, B. M., Pierre, V. C. & Barton, J. K. Metallo-intercalators and metallo-insertors. *Chem. Commun.* **44**, 4565–4579 (2007).
29. Prieto Otoya, T. D. et al. Re-pairing DNA: binding of a ruthenium phi complex to a double mismatch. *Chem. Sci.* **15**, 9096–9103 (2024).
30. Walt, D. R. Optical methods for single molecule detection and analysis. *Anal. Chem.* **85**, 1258–1263 (2013).
31. Rye, H. S. et al. Stable fluorescent complexes of double-stranded DNA with bis-intercalating asymmetric cyanine dyes: properties and applications. *Nucleic Acids Res.* **20**, 2803–2812 (1992).
32. Perkins, T. T., Smith, D. E., Larson, R. G. & Chu, S. Stretching of a single tethered polymer in a uniform flow. *Science* **268**, 83–87 (1995).
33. Sischka, A. et al. Molecular mechanisms and kinetics between DNA and DNA binding ligands. *Biophys. J.* **88**, 404–411 (2005).
34. Hanwell, M. D., Curtis, D. E., Lonie, D. C. & Vandermeersch, T. Avogadro: an advanced semantic chemical editor, visualization, and analysis platform. *J Cheminformatics* **4**, 17 (2012).
35. Messina, M. S. et al. A histochemical approach to activity-based copper sensing reveals cuproplasia-dependent vulnerabilities in cancer. *Proc. Natl. Acad. Sci. USA* **122**, e2412816122 (2025).
36. Kastan, M. B. & Bartek, J. Cell-cycle checkpoints and cancer. *Nature* **432**, 316–323 (2004).
37. Gałczyńska, K. et al. Copper(II) complex with 1-allylimidazole induces G2/M cell cycle arrest and suppresses A549 cancer cell growth by attenuating Wnt, JAK-STAT, and TGF-β signaling pathways. *J. Inorg. Biochem.* **264**, 112791 (2025).
38. Molinaro, C. et al. A novel copper(II) indenoisoquinoline complex inhibits topoisomerase I, induces G2 phase arrest, and autophagy in three adenocarcinomas. *Front. Oncol.* **12**, 837373 (2022).
39. Hilbert, B. J., Hayes, J. A., Stone, N. P., Xu, R.-G. & Kelch, B. A. The large terminase DNA packaging motor grips DNA with its ATPase domain for cleavage by the flexible nuclease domain. *Nucleic Acids Res* **45**, 3591–3605 (2017).
40. Zuin Fantoni, N. et al. Polypyridyl-based copper phenanthrene complexes: a new type of stabilized artificial chemical nuclease. *Chem. Eur. J.* **25**, 221–237 (2019).
41. Molphy, Z. et al. Copper phenanthrene oxidative chemical nucleases. *Inorg. Chem.* **53**, 5392–5404 (2014).
42. Detinis Zur, T., Deek, J. & Ebenstein, Y. Single-molecule approaches for DNA damage detection and repair: a focus on repair assisted damage detection (RADD). *DNA Repair* **129**, 103533 (2023).
43. Su'etsugu, M. & Errington, J. The replicase sliding clamp dynamically accumulates behind progressing replication forks in Bacillus subtilis cells. *Mol. Cell* **41**, 720–732 (2011).
44. Santoro, A. et al. The glutathione/metallothionein system challenges the design of efficient O_2-activating copper complexes. *Angew. Chem. Int. Ed Engl.* **59**, 7830–7835 (2020).
45. Rigaku Oxford Diffraction, CrysAlisPro Software system, Version 1.171.43.115a, Rigaku Corporation, Wroclaw, Poland (2024).
46. Hübschle, C. B. ShelXle: a Qt graphical user interface for SHELXL. *Acta Crystallogr. A Found. Adv.* **75**, a187–a187 (2019).
47. Dolomanov, O. V., Bourhis, L. J., Gildea, R. J., Howard, J. & Puschmann, H. OLEX2: a complete structure solution, refinement and analysis program. *J. Appl. Crystallogr.* **42**, 339–341 (2009).
48. Sheldrick, G. M. SHELXT - integrated space-group and crystal-structure determination. *Acta Crystallogr. A Found. Adv.* **71**, 3–8 (2015).
49. Sheldrick, G. M. Crystal structure refinement with SHELXL. *Acta Crystallogr. C Struct. Chem.* **71**, 3–8 (2015).
50. McCann, M. et al. A new phenanthroline-oxazine ligand: synthesis, coordination chemistry and atypical DNA binding interaction. *Chem. Commun.* **49**, 2341–2343 (2013).
51. Frykholm, K., Müller, V., Sriram, K. K. Dorfman, K. D. & Westerlund, F. DNA in nanochannels: theory and applications. *Q. Rev. Biophys.* **55**, e12 (2022).
52. Sriram, K. K. et al. Fluorescence microscopy of nanochannel-confined DNA. *Methods Mol. Biol.* **2694**, 175–202 (2024).
53. Trott, O. & Olson, A. J. AutoDock Vina: improving the speed and accuracy of docking with a new scoring function, efficient optimization, and multithreading. *J. Comput. Chem.* **31**, 455–461 (2010).
54. Abraham, M. J. et al. GROMACS: high performance molecular simulations through multi-level parallelism from laptops to supercomputers. *SoftwareX* **1–2**, 19–25 (2015).
55. Van Der Spoel, D. et al. GROMACS: fast, flexible, and free. *J. Comput. Chem.* **26**, 1701–1718 (2005).
56. Huang, J. et al. CHARMM36m: an improved force field for folded and intrinsically disordered proteins. *Nat. Methods* **14**, 71–73 (2017).
57. Wang, J., Wang, W., Kollman, P. A. & Case, D. A. Automatic atom type and bond type perception in molecular mechanical calculations. *J. Mol. Graph. Model.* **25**, 247–260 (2006).
58. Salentin, S., Schreiber, S., Haupt, V. J., Adasme, M. F. & Schroeder, M. PLIP: fully automated protein-ligand interaction profiler. *Nucleic Acids Res.* **43**, W443–W447 (2015).

Acknowledgements

We acknowledge funding from Research Ireland (12/RC/2275_P2), the Irish Research Council (IRCLA/2022/3815), and the Novo Nordisk Foundation (NNF19OC0056845). We also acknowledge the European Union's Horizon 2020 research and innovation program under the Marie Sklodowska-Curie grant agreement No 861381 (NATURE-ETN). We are grateful for financial support from the ANR (ANR-20-CE07-0035), the ERC Consolidator Grant PhotoMedMet to G.G. (GA 681679), the program "Investissements d' Avenir" launched by the French Government and implemented by the ANR with the reference ANR-10-IDEX-0001-02 PSL (G.G.). F.W. acknowledges funding from the European Research Council (ERC consolidator, grant no 866238), the Swedish Research Council (grant no. 2020–03400), the Swedish Cancer Foundation (grant no. 201145 PjF) and the Swedish Child Cancer Foundation (grant no. PR2022-001). The nanofluidic devices used in this study were fabricated at MyFab Chalmers cleanroom facility. P.J. acknowledges funding from the Swedish Child Cancer Foundation (grant no. 2022-0010), Jubileumsklinikens Cancerfond (2023:504).

Author contributions

A.G., M.S., E.D., P.M., L.A., S.K.K., O.A.A., H.H., F.F. and K.C. conducted experiments. A.G. and A.K. wrote the manuscript and prepared figures. V.M., P.J., S.B., D.T., M.W., G.G., F.W. and A.K. provided supervision. All authors assisted with manuscript review and revision. A.G. and A.K. conceptualised the study.

Competing interests
The authors declare no competing interests.

Additional information
Supplementary information The online version contains supplementary material available at https://doi.org/10.1038/s41467-026-68911-5.

Correspondence and requests for materials should be addressed to Andrew Kellett.

Peer review information *Nature Communications* thanks Sherif Shaban Ragab and the other, anonymous, reviewer(s) for their contribution to the peer review of this work. A peer review file is available.